ORIGINAL RESEARCH ARTICLE

Formation of Coarse Recrystallized Grains in 6016 Aluminum Alloy During Holding After Hot Deformation

SAOUSSEN OUHIBA, ALEXIS NICOLAY, LAURENT BOISSONNET, MARC BERNACKI, and NATHALIE BOZZOLO

Controlling the grain size of recrystallized grains during hot rolling is crucial in 6xxx aluminum alloys used in automotive applications to avoid the development of roughness on the surface of the formed sheet. The possible factors responsible for the development of coarse recrystallized grains are investigated in this paper. With this aim, hot compression tests followed by post-deformation holding in the testing furnace as well as by sequential annealing in the SEM chamber are performed and the evolution of the microstructure is characterized using EBSD. Grain overgrowth takes place in both types of experiments. The investigation shows that stored energy is the key factor behind the overgrowth of some recrystallized grains at the expense of others and that Smith–Zener pinning is unable to prevent this phenomenon because of the high driving pressure associated with stored energy. The anisotropic characteristics and behavior of coarse recrystallized grain boundaries are also studied. It comes out that the misorientation angle and axis are not sufficient to determine grain boundary migration rate.

https://doi.org/10.1007/s11661-022-06672-8

I. INTRODUCTION

6XXX aluminum alloys are attracting considerable interest in the automotive industry due to their light-weight properties contributing to a significant decrease in the fuel consumption and CO_2 emissions. These alloys offer good properties such as formability, corrosion resistance, weldability and strength. An additional requirement consisting in the surface appearance needs to be met so that these alloys can be used for outer car body panels. Unfortunately, some 6xxx alloys are prone to roping, which is represented by a series of visible ridges and valleys on the stamped sheet surface. These surface defects cannot be covered even after painting, making these parts inappropriate for aesthetic reasons.[1–3]

This roping phenomenon has been attributed to the formation of coarse grains during hot rolling or intermediate annealing. These coarse grains are then drawn out into elongated areas during cold rolling, which will subsequently recrystallize into a finer grain structure. This results in the formation of bands of similarly oriented recrystallized grains, that correspond to the lines observed on the stamped sheet.[4] Hence, it is important to control recrystallization during and after the hot rolling process to avoid these coarse grains' formation, and in turn these surface defects.

Coarse recrystallized grains have been observed in different materials, including aluminum alloys,[5–11] nickel-based superalloys[12–15] and electrical steels.[16] The velocity of a grain boundary is generally described by $V = MP = M(P_{SE} - P_Z - P_C)$, where M is the boundary mobility and P is the net driving pressure, which is the net sum of the stored energy difference P_{SE}, capillarity P_C and Smith–Zener pinning pressure P_Z.[17] A higher boundary velocity is caused therefore by a higher boundary mobility and/or a higher net driving pressure. The possible metallurgical factors contributing to the development of coarse recrystallized grains are the following:

- A heterogeneous distribution of stored energy through dislocation accumulation: It is known that high gradients of stored energy are responsible for nucleation and growth of recrystallized grains. In the case of small deformations, the stored energy can be heterogeneously distributed within the deformed microstructure, which can produce a limited number

SAOUSSEN OUHIBA, ALEXIS NICOLAY, MARC BERNACKI, and NATHALIE BOZZOLO are with the MINES ParisTech, PSL-Research University, CEMEF-Centre de mise en forme des matériaux, 06904 Sophia antipolis, France. Contact e-mail: saoussen.ouhiba@minesparis.psl.eu LAURENT BOISSONNET is with the C-TEC Constellium Technology Center, 38341 Voreppe, France.

Manuscript submitted December 3, 2021; accepted March 21, 2022.

Published online: 19 April 2022

of active nucleation sites and/or then a selective growth of low stored energy grains[5,12–15];

- A heterogeneous Smith–Zener pinning pressure: Coarsening or dissolving second-phase particles can lead to a variable pinning pressure and therefore to abnormal grain growth or to coarse recrystallized grains.[12,18–20] Concurrent precipitation occurring during annealing has been also reported as responsible for the formation of coarse recrystallized grains.[9,10] Indeed, non-isothermal annealing of cold rolled Al–Mn–Fe–Si alloy has been found to promote the formation of an elongated and coarse grain structure with a stronger P texture due to the dispersoids that form preferentially at high angle grain boundaries and later on low angle grain boundaries before the onset of recrystallization. Nucleation at grain boundaries is thus inhibited and only few P oriented grains can grow out of the deformation zone due to their special boundary characteristics with respect to the surrounding deformed matrix, leading to a strong P texture component and to a coarse pancake grain structure.[9,10] A locally low Smith–Zener pinning pressure in the neighborhood of a recrystallized grain can be easily overcome by the driving pressure for grain boundary migration and, therefore, can induce grain overgrowth.[13,21] Finally, it has been reported that a non-random distribution of second-phase particles can also promote abnormal grain growth, larger grains being found in regions of lower particle density[6];
- Heterogeneous grain boundary properties associated with non uniform grain boundary character distributions (GBCDs): Both mobility and energy depend on the structure of the grain boundary, that is very dependent on the misorientation and the inclination of grain boundary plane.[22,23] The evolution of the orientation distribution of recrystallized grains in commercial purity Al (AA1145) with increasing annealing time has been studied by EBSD by Engler *et al.*[24] and it has been found that a higher mobility can be attributed to a special misorientation relationship (*e.g.,* 40deg $\langle 111 \rangle$) between the recrystallized grain and the deformed matrix.[24] Highly textured materials are also often subjected to abnormal grain growth due to the high number of low-angle boundaries between similarly oriented grains. Therefore, grains outside the dominant texture components have high angle grain boundaries that are generally characterized by a high mobility, allowing them to overgrow.[8,12,13,24] In addition, preferential growth of grains having boundaries with low energy has been reported by References 16, 25–27. In these studies, it has been shown that, if a grain has a high fraction of low energy boundaries, it can grow abnormally by the capillarity effect through an evolution denominated as solid state wetting.
- Heterogeneous grain boundary properties associated with non uniform solute drag: The mobility advantage for some grain boundaries can be due to a lower solute drag effect. According to Huang *et al.*,[28] the mobility of grain boundaries in Al–Mg alloys decreases rapidly with increasing solute concentration and depends mainly on solute concentration and temperature regardless of the solute type.[28] The role of solute drag in the occurrence of abnormal grain growth has been examined by Kim *et al.*[29] by simulating grain growth in presence of grain boundary segregation using a phase field model. It has been shown that the solute drag effect can induce abnormal grain growth even in homogeneous polycrystalline systems without any texture, anisotropic grain boundary properties, second-phase particles and grain size advantage.[29]

Thus, due to the large number of parameters that may affect the grains' evolution, it is challenging to determine precisely the underlying mechanisms behind the formation of coarse recrystallized grains. The peripheral coarse recrystallized grains formed during extrusion in 6xxx aluminum alloys have been extensively studied[30–32] and it has been reported that the mechanism responsible for the formation of these peripheral coarse recrystallized grains is not fully understood as it depends on the local stored energy, the thermal conditions and the retarding pressure from second-phase particles. However, the formation of coarse recrystallized grains at the core region after hot rolling has not been extensively studied and is still not well understood. In addition, abnormal grain growth (*i.e.*, capillarity-driven growth of a few grains in the absence of a stored energy)[6–8,33] has been more studied than recrystallized grain overgrowth (*i.e.*, growth of a few grains driven by stored energy)[5,34] in aluminum alloys.

The present study aims therefore to improve the understanding of the formation of coarse recrystallized grains in 6016 aluminum alloys after hot rolling process. Hot compression tests followed by different holding times, as well as sequential annealing on deformed and water quenched samples, were performed in order to describe the appearance and evolution of the coarse recrystallized grains. The results are analyzed and discussed in the light of the possible causes for grain overgrowth detailed above.

II. EXPERIMENTAL PROCEDURE AND DATA PROCESSING METHODS

A. *Material*

The material of interest is a 6016 aluminum alloy provided by C-TEC Constellium Technology Center, Voreppe. The standard chemical composition for AA6016 is given by Table I. The main alloying elements are Si, Mg, Cu, and Mn. The studied material also contains unavoidable Fe traces. The second-phase particles that are expected to be present in this alloy are Fe containing intermetallic particles, soluble phases (*i.e.,* Mg_2Si/Si particles) and Mn dispersoids.

Table I. Chemical Composition (Wt Pct) for 6016 Aluminum Alloy[1]

Alloy	Mg	Si	Cu	Fe	Mn	Zn	Ti
AA6016	0.25–0.6	1.0–1.5	<0.2	<0.5	<0.2	<0.2	<0.15

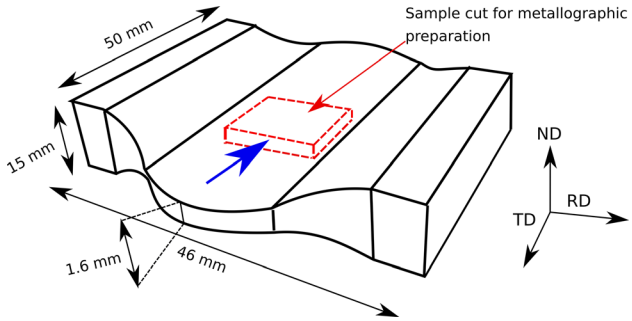

Fig. 1—Schematic drawing showing a hot-compressed specimen and the location where a sample for EBSD characterization is cut. The sample surface that is prepared for microstructure analysis is shown by the blue arrow (Color figure online).

Hot compression specimens of 46 mm (in the rolling direction RD), 50 mm (in the transverse direction TD) and 15 mm (in the normal direction ND) were machined from $\frac{1}{4}$ thickness of an as-cast ingot. Prior to hot compression, the specimens were subjected to homogenization followed by a particular subsolvus thermal process aiming at generating a significant precipitation of the soluble phases and thus at impoverishing the solid solution. The RD, TD and ND refer to the directions of the sample after hot compression.

B. *Thermomechanical Path*

The specimens were compressed using a Servotest thermomechanical plane compression machine at a temperature of 430 °C, at a strain rate of $3\,s^{-1}$, and to a strain of 2.4. These conditions were preliminarily identified as promoting the formation of coarse recrystallized grains during post-deformation annealing. Some specimens were subsequently quickly water quenched to freeze the deformed microstructure. Other samples were kept at 430 °C after deformation for different holding times before water quench to investigate post-dynamic microstructure evolutions.

C. *Sample Preparation*

1. *For EBSD characterization*

After hot compression tests, sections were cut along the RD–ND plane at the centre of the compression specimens as shown in Figure 1 and were mechanically polished down to 0.05 μm colloidal silica suspension. For Electron Backscatter Diffraction (EBSD) measurements, the samples were subsequently electropolished (48 V, 0 °C) for 10 seconds using the electrolytic solution A2 provided by Struers. A Zeiss Supra40 scanning electron microscope (SEM) was used for running EBSD analyses with a Bruker system. At least five EBSD orientation maps, with a size of 1200 μm (RD) × 800 μm (ND) each and a measurement step size of 3 μm, were taken at the mid-thickness of the samples and stitched together to study texture. Higher magnification and spatial resolution EBSD orientation maps were also acquired when needed. MTEX Toolbox[35] was finally used for EBSD data processing and analysis.

2. *For quantification of precipitates*

For quantitative analysis of precipitates, the sectioned samples were mechanically polished following a specific internal procedure, and then ion milled using the Gatan Ilion II device. Afterward, SEM in-lens Secondary Electron (SE) and Backscattered Electron (BSE) images were acquired using a Zeiss Ultra55 SEM equipped with the software SmartStitch, allowing automatic acquisition and stitching of multiple images. A total area of 1600 μm (RD) × 600 μm (ND) was analyzed to obtain representative statistics. The pixel resolution of the stitched image was $40,960 \times 15,360$. The smallest detectable particle had an equivalent circle diameter of 62 nm.

The advantage of such a method is that it distinguishes clearly between the different types of precipitates and the matrix and therefore quantifies with more accuracy the mean size and area fraction of these particles. The stitched in-lens SE and BSE images were subsequently processed using MATLAB R2018a.

3. *For sequential annealing using a fast heating stage coupled to SEM*

A 6 mm (RD) × 4.5 mm (TD) sample was cut at mid-thickness of a previously deformed and water quenched sample. First, the sample was polished on both sides to avoid recrystallization to be initiated from the backside. Second, the sample was mounted and mechanically polished down to a thickness of 300 μm. The polishing process included polishing using diamond suspensions followed by vibratory polishing in a 0.05 μm colloidal silica suspension for 3 hours to achieve an excellent surface quality required for EBSD measurements. Electropolishing was avoided for preparing this sample because it reveals precipitates on top of the prepared surface with possible influence on the Smith-Zener pinning force acting on migrating boundaries at the sample surface.

A fast heating stage was mounted inside the chamber of a Tescan FERA3 FIB-SEM equipped with an Oxford EBSD system. The working principle of the heating stage is the same as the one described in References 36, 37. The sample surface was point-welded on the heating

device, consisting of a thin tantalum ribbon and temperature was measured with two thermocouples welded on the top surface of the sample, as shown in Figure 2(a). The tantalum ribbon was heated by Joule effect. The small dimensions of both tantalum ribbon and sample ensure low thermal inertia and therefore allow high heating and cooling rates ($\approx 100°Cs^{-1}$). The observed zone was chosen at a certain distance from the welding points to avoid the impact of welding on the microstructure.

A series of nine successive thermal cycles with intermediate EBSD measurements were performed, as shown in Figure 2(b). After each annealing step, EBSD orientation maps with a step size of 3 μm were acquired next to each other and stitched together to cover a wide total area of 4 mm (RD) $\times$ 2 mm (TD). Such large analyzed area allows to follow the growth of a significant number of recrystallized grains and, notably, to investigate the influence of the grain boundary misorientation on recrystallization.

Microstructure analysis on the RD–TD plane is necessary in our case because of an experimental constraint related to the sequential annealing setup and the dimensions of the compressed sample.

The advantage of the sequential annealing coupled to EBSD is the possibility of keeping the same area of observation and therefore following the evolution of individual coarse recrystallized grains in time. However, it is important to keep in mind that results may be influenced by artifacts due to free surface effects.[36,37]

D. *EBSD Data Analysis*

1. *Definition of recrystallized grains*

The raw EBSD data sets were at first filtered using the local linear adaptation of smoothing splines (LLASS) filter,[38] which is implemented within the MTEX toolbox.[35] This filter allows decreasing the orientation noise and improving the angular resolution of intragranular misorientations.[38,39]

Individual grains were identified from the EBSD data as having a minimum size of 12 pixels (*i.e.,* a minimum equivalent circle diameter of about 12 μm when using a step size of 3 μm, 4 μm with a step size of 1 μm and 1.5 μm with a step size of 0.4 μm). The pixels assigned to the same grain have a point to point misorientation lower than 10 deg.

The grain average misorientation (GAM), defined as the average of the misorientation angle between each pair of neighboring pixels within a grain, was used in order to separate recrystallized grains from deformed ones. First, for the determination of the GAM value of each grain, the Kernel average misorientation (KAM) of each pixel in the grain was calculated and the average of all these calculated KAM values gave the GAM value of the considered grain. A threshold and a kernel size were required for the calculation of KAM values. In this case, the threshold was set to 10 deg to exclude grain boundaries from contributing to the KAM calculation and a 2nd order kernel was used (*i.e.,* both first and second nearest neighbors were considered). Second, the threshold value of GAM used to distinguish between recrystallized and deformed grains was adjusted according to the EBSD measurement step. Here, for a measurement step size of 0.4 μm, a GAM value lower than 0.4 deg was considered in order to determine recrystallized grains. For a measurement step size of 1 μm, a GAM value lower than 0.8 deg was considered. And finally, for a measurement step size of 3 μm, a GAM value lower than 1.2 deg was considered.

The grain size was determined as the equivalent circle diameter (*i.e.*, the diameter of a disk having the same area as the grain). The average grain size was therefore the arithmetic average value of equivalent circle diameters calculated for all the considered grains.

2. *Texture components in aluminum alloys*

The typical deformation and recrystallization texture components that may appear in aluminum alloys are summarized in Table II.

The area fractions of recrystallized grains belonging to the typical texture components are calculated at different holding times after deformation based on EBSD data. A grain is classified as belonging to a specific texture component if its orientation is within a 10 deg deviation with respect to the rotation axis from the ideal texture component. The area fraction of a

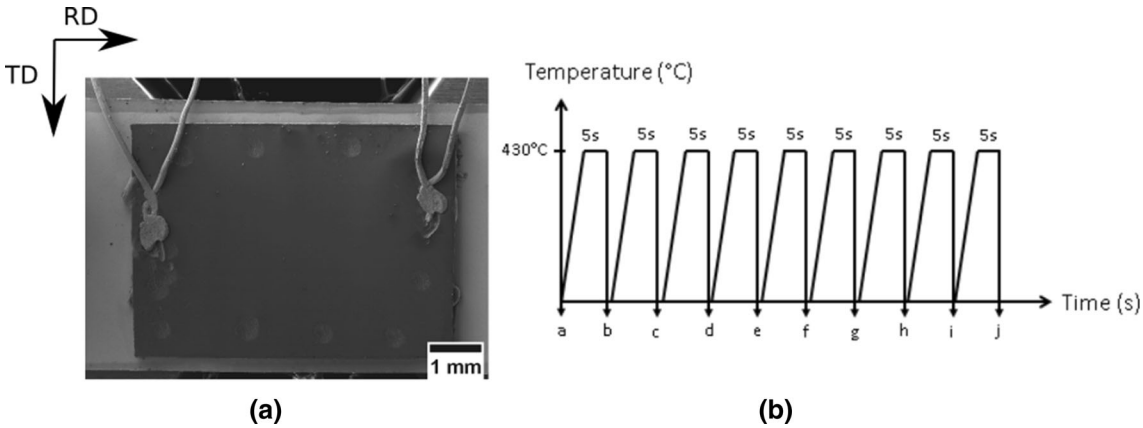

Fig. 2—(*a*) Thermocouples welded on the sample intended for sequential annealing, (*b*) schematic representation of the sequential annealing applied using the fast heating stage coupled to SEM.

Table II. Euler Angles of Typical Texture Components in Aluminum Alloys Following Bunge's Convention[40]

Designation	$\phi 1$ (deg)	Φ (deg)	$\phi 2$ (deg)
Goss	0	45	0
Cube	0	0	0
CubeND45	45	0	0
CubeRD20	0	22	0
CubeND18	18	0	0
Copper	90	35	45
Brass	35	45	0
S	53	35	63

The sample reference frame is {RD,TD,ND}.

texture component within the recrystallized grains is calculated as the area of grains belonging to a specific texture component divided by the area of all recrystallized grains. The same approach is followed for the calculation of area fractions of deformed grains belonging to the main texture components.

E. *Image Analysis for Quantification of Second-Phase Particles*

As mentioned in Section II–C–2, the stitched in-lens SE and BSE images were processed using MATLAB R2018a. More specifically, for quantification of Mg_2Si and Si particles, the stitched in-lens SE image was analyzed as shown in Figure 3(a). Mg_2Si and Si particles appear gray and black in the stitched in-lens SE image, respectively. For quantification of dispersoids and Fe containing particles, the stitched BSE image was analyzed as shown in Figure 3(b). Both fine dispersoids and large Fe containing particles appear white in the stitched BSE image. The stitched BSE image was chosen instead of the stitched in-lens SE image for determination of dispersoids and Fe containing particles because of the better contrast between these particles and the dark background. For processing both stitched in-lens SE and BSE images, the contrast was adjusted and the noise was reduced by adding a salt and pepper noise followed by a median filter (*i.e.,* replacing each pixel by the median value of a 3 by 3 neighborhood around the corresponding pixel). The particles were subsequently identified based on their gray level as can be seen in Figure 3. The particle size was determined as the equivalent circle diameter. The area fraction of all particles without any distinction was calculated by adding their areas and dividing by the total analyzed area.

F. *Estimation of Driving Pressures Acting on Grain Boundaries*

At the mesoscopic scale, the grain boundary velocity (V) is generally assumed to be well approximated by the equation $V = MP$ with M the grain boundary mobility and P the net driving pressure. A higher boundary migration rate can be then related either to a higher mobility (M) or to a higher net driving pressure (P). A brief description of how to roughly estimate the net driving pressure is summarized below. The net driving pressure P in the early stage of recrystallization can be expressed as follows[17]:

$$P = P_{\mathrm{SE}} - P_Z - P_C\,, \qquad [1]$$

where P_{SE} is the driving pressure due to stored energy, P_Z is the Smith–Zener pinning pressure due to second-phase particles and P_C is the capillarity pressure due to boundary curvature.

The grain size distribution is determined from a 2D EBSD map. Similarly, the second-phase particle distribution is determined from 2D SEM micrographs. Therefore, the pressures controlling the migration of grain boundaries are determined in 2D context.

The driving pressure due to the difference in stored energy between a grain G_i and a grain G_j can be expressed using the following formula[17]:

$$P_{SE} = E_j - E_i \text{ with } \mathrm{E_i} = 0.5\,\rho_{\mathrm{i}}\,\mathrm{G\,b^2} \quad \forall \mathrm{i}\,, \qquad [2]$$

where E_i is the stored energy of grain G_i (per unit volume), ρ_i is the average total dislocation density in grain G_i, b is the magnitude of Burgers vector (= 0.286 nm for pure aluminum[17]) and G is the shear modulus (= 26.1 GPa[5]).

Dislocations are classified into statistically stored dislocations (SSD) and geometrically necessary dislocations (GND). SSDs have a net zero Burgers vector and thus do not promote lattice curvature at the microscopic scale. They are therefore impossible to assess from EBSD data. For this reason, as a rough estimation, we will consider that SSDs represent a certain fraction of the total density of dislocations. Thus, ρ_i can be approximated as[41]:

$$\rho_i = \rho_{\mathrm{GND_i}} + \rho_{\mathrm{SSD_i}} = c\,\rho_{\mathrm{GND_i}} = c\,\frac{K\theta_i}{b\,x}\,, \qquad [3]$$

where c is a constant higher than 1, K is a parameter depending on the assumed type of dislocation structures (= 3 in case of parallel edge dislocations according to Reference 41), θ_i is the misorientation angle between two pixels separated by a distance x and x is the distance over which the misorientation angle is calculated.

By taking into account Eqs. [2] and [3], the driving pressure due to the difference in stored energy between grain G_i and grain G_j can be calculated as follows:

$$\begin{aligned} P_{\mathrm{SE}} &= 0.5\left(\rho_j - \rho_i\right) G b^2 \\ &= 0.5\,\frac{cK\left(\theta_j - \theta_i\right) G b}{x} \\ &= \frac{c3\left(\theta_j - \theta_i\right) G b}{2x} \end{aligned} \qquad [4]$$

In the present study, the driving pressure for the migration of recrystallized grain boundaries is estimated in order to determine whether stored energy contributes to the overgrowth of recrystallized grains. For this purpose, the difference in stored energy between each recrystallized grain and its neighborhood is calculated as follows:

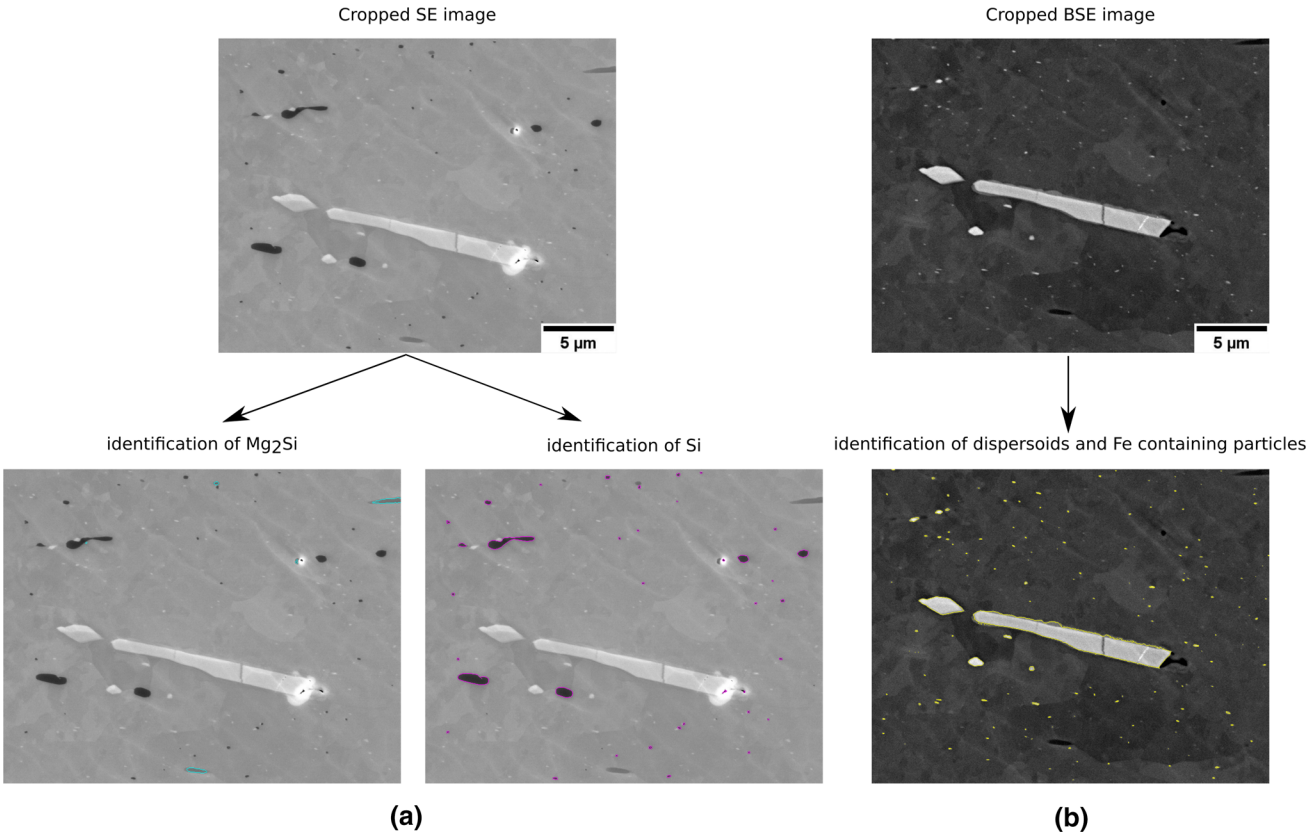

Fig. 3—Identification of precipitates for quantification: (*a*) a cropped area from the stitched in-lens SE image showing how Mg_2Si and Si particles are identified and (*b*) the same cropped area from stitched BSE image showing how fine dispersoids and large Fe containing particles are identified.

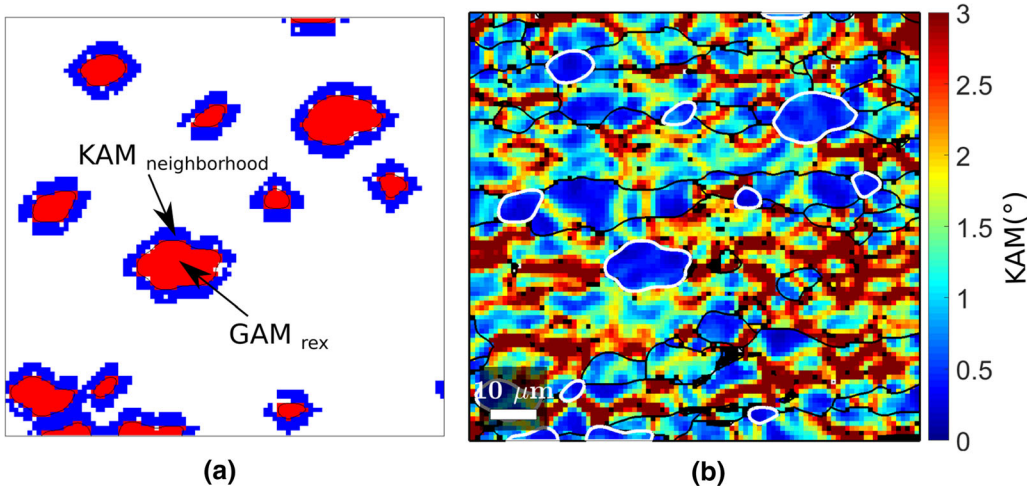

Fig. 4—(*a*) Schematic image showing the 3 pixel thick deformed neighborhood (blue) around each recrystallized grain (red), as considered for estimating the local driving force associated with stored energy. (*b*) Corresponding KAM map showing recrystallized grain boundaries in white lines and deformed grain boundaries in black lines (Color figure online).

$$PSE = \frac{c\,3\,(\,\theta_{neighbor} - \theta_{rex}\,)\,G\,b}{2\,x} \qquad [5]$$

GAM_{rex}, equivalent to the average of KAM values in a recrystallized grain, is chosen in order to estimate the average θ_{rex} value (see Figure 4(a)). However, because of the strong heterogeneity of the strain field at the intra- and intergranular scales (see Figure 4(b)), the neighborhood of each recrystallized grain is set to a three pixels width for the estimation of $\theta_{neighbor}$ as can be shown in Figure 4(a). A neighborhood of a width of 3 pixels is selected as a good compromise after trying several

thicknesses. The average of the KAM values of all the pixels included in the neighborhood ($\overline{KAM}_{neighbor}$) is calculated. $\theta_{neighbor} - \theta_{rex}$ can therefore be replaced by $\overline{KAM}_{neighbor} - GAM_{rex}$ in Eq. [5]. In this case, a threshold of 10 deg and a 1st order kernel where only the first neighbors are considered are used to calculate KAM values and therefore $\overline{KAM}_{neighbor}$ and GAM_{rex}. Finally, the x value in Eq. [5] must be taken as equal to the EBSD measurement step size.

The Smith–Zener pinning pressure can be approximated by the following expression[17]:

$$P_Z = \frac{3\gamma f_{spp}}{d_{spp}}, \quad [6]$$

where $fspp$ is the precipitate area fraction, $dspp$ is the precipitate average equivalent diameter in 2D and γ is the grain boundary energy ($0.324\,J/m^2$ for pure aluminum.[28])

Finally, the pressure due to the curvature of recrystallized grain boundaries can be estimated by:

$$P_C = \frac{\gamma}{R_{rex}}, \quad [7]$$

where R_{rex} is the mean recrystallized grain radius in 2D.

III. RESULTS AND DISCUSSION

A. *Initial Microstructure*

Figure 5 shows the initial precipitation state, which consists mainly of elongated Fe containing intermetallic particles decorating grain boundaries and intragranular fine Mg_2Si/Si particles.

Figure 6 illustrates the initial microstructure, which is homogeneous and fully recrystallized with equiaxed grains having an average equivalent diameter of about 116 μm with a standard deviation of 57 μm. The {111} pole figure of the initial microstructure shown in Figure 6 demonstrate that there is no preferential orientation for the initial grains.

B. *Microstructure Evolution During Post-deformation Holding*

1. *Microstructure right after hot deformation*

The microstructure quenched right after hot compression (actually 2 seconds after the end of deformation) is shown in Figure 7. The EBSD orientation map shown in Figure 7(a) was taken in the plane RD–ND, whereas the EBSD orientation map shown in Figure 7(b) was taken in the plane RD–TD. A zoom onto a selected area in both EBSD orientation maps shows that dynamically recrystallized (DRX) and post-dynamically recrystallized (PDRX) grains coexist. Unlike the PDRX grains, the DRX grains are the ones that have inhomogeneous orientation, thus that contain substructures (indicated by black arrows on Figure 7). The presence of recrystallized grains with no measurable intragranular misorientations is interpreted here to be the result of PDRX, which occurred during the 2 seconds of quenching delay. PDRX can indeed be very fast after deformation at such strain rates.[42]

The texture of recrystallized grains as well as that of deformed matrix are shown in Figure 8. The recrystallized grains do not exhibit any strong preferred orientation while the deformed grains are mostly Brass and Goss oriented. The average equivalent diameter of recrystallized grains including both DRX and PDRX ones is about 7.0 μm with a standard deviation of 2.8 μm in the plane RD–ND, while it is about 7.7 μm with a standard deviation of 3.5 μm in the plane RD–TD.

2. *Post-dynamic appearance of coarse recrystallized grains*

The evolution of the deformed microstructure during longer holding times before quenching is shown on Figure 9. Similarly, the evolution of a region of interest (ROI) in the RD–TD plane during sequential annealing using a heating stage in the SEM chamber is shown in Figure 10. Grain overgrowth occurs in both types of experiments. A comparison between the recrystallization fractions obtained during both types of experiments (see Figure 11) shows a similar behavior, confirming that surface effects on recrystallization rates in the sequential annealing series were negligible in the presence of stored energy.

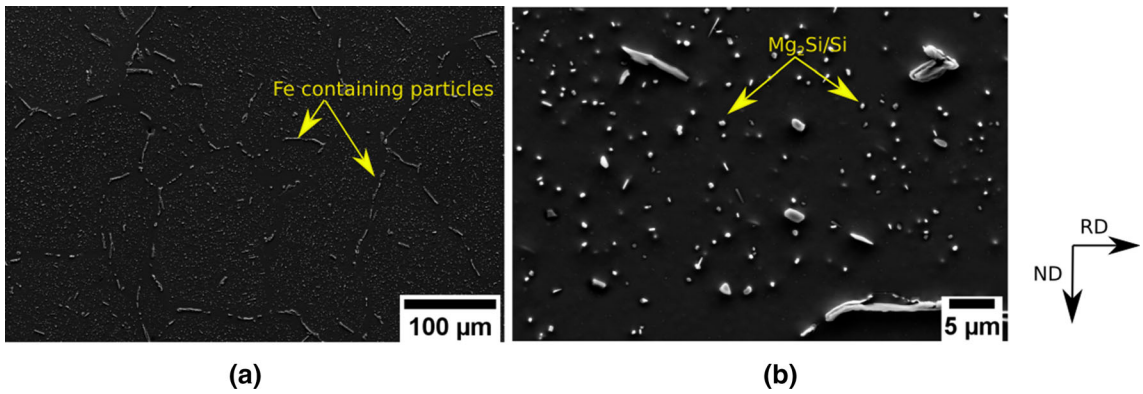

Fig. 5—(*a*) Low and (*b*) high magnification SEM SE images showing the precipitation content in the initial state.

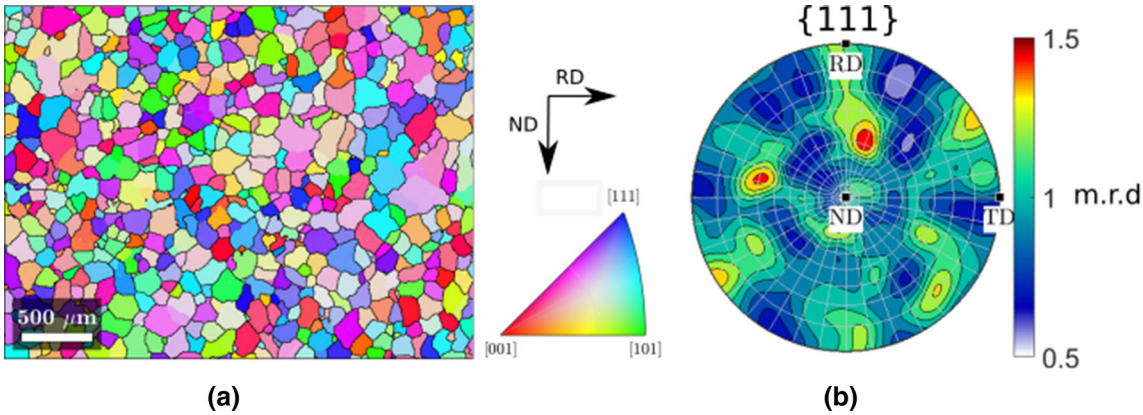

Fig. 6—(*a*) EBSD orientation map showing the initial microstructure. The grain boundaries are plotted in black. The color code defined on the standard triangle refers to the normal direction. The measurement step size is 5 μm, (*b*) the corresponding {111} pole figure. The texture intensity is expressed in multiple of random distribution (m.r.d) (Color figure online).

3. *Shape of coarse recrystallized grains*

The coarse recrystallized grains possess an elongated shape when they are observed in the RD–ND plane as seen in Figure 9(d). However, when they are examined in the RD-TD plane, they are less elongated (see Figure 10(j)), suggesting that the coarse recrystallized grains develop more in the RD and TD than in the ND.

C. *Texture of Coarse Recrystallized Grains*

The evolution of texture of coarse recrystallized grains during post-deformation holding is shown in Figure 12(a). It is clear that the coarse recrystallized grains have mostly a "near Cube" orientation (*i.e.*, Cube, Cube rotated about 18 deg around ND and Cube rotated about 20 deg around RD), meaning that "near Cube" oriented grains develop preferentially compared to other-oriented grains. It is nevertheless important to notice a wide scatter around the ND and the RD for those "near Cube" orientations.

The texture of coarse recrystallized grains obtained after 40 seconds of sequential annealing is compared with the one obtained after 40 seconds of post-deformation holding (see Figure 12(b)). A weaker "near Cube" texture is found for coarse recrystallized grains during sequential annealing, as can be seen also from the {111} pole figure shown in Figure 10(j) in comparison with Figure 9(d)). This could possibly be a statistical effect associated with the lower number of grains available in the sequential annealing experiment.

It is important to note also that the large recrystallized grains, observed at the plane RD–ND after holding for 120 seconds and having a "near Cube" orientation, represent only 40 pct of all large recrystallized grains (see Figure 12(a)), meaning that "near Cube" oriented recrystallized grains are not the only grains that can overgrow. Other-oriented recrystallized grains can also overgrow to reach abnormally large sizes.

D. *Exploring Possible Factors Leading to Grain Overgrowth*

The origin of Cube orientation has been extensively studied in the past in different materials including copper,[43] Al–Mn–Mg alloys[44,45] and commercial purity aluminum.[46,47] However, there is still debate about it.[48] This section aims to discuss the factors possibly leading to the overgrowth of "near Cube" oriented grains in the studied alloy.

1. *Initial size advantage of "near Cube" oriented recrystallized grains*

One possible explanation of "near Cube" oriented grain overgrowth is that "near Cube" oriented subgrains dynamically recover more rapidly than other orientations, achieving therefore a low stored energy configuration that allows them to bulge out as DRX or PDRX "near Cube" nuclei from the very beginning of recrystallization. Such faster dynamic recovery would give rise to a size advantage for the "near Cube" recrystallized grains present at the end of deformation (*i.e.,* after deformation and quenching). The size distribution of both "near Cube" and other-oriented recrystallized grains examined right after deformation is displayed on Figure 13. The mean size for "near Cube" oriented recrystallized grains ($\approx$ 9 μm) is indeed slightly higher than for other-oriented recrystallized grains ($\approx$ 7 μm). The size distribution of "near Cube" oriented recrystallized grains is ranging from 5 to 25 μm, while the size distribution of other-oriented recrystallized grains is ranging from 4 to 30 μm. This means that the largest recrystallized grain obtained right after deformation does not necessarily have a "near Cube" orientation. Therefore, initial size advantage is unlikely to be sufficient to explain the growth advantage of "near Cube" oriented recrystallized grains.

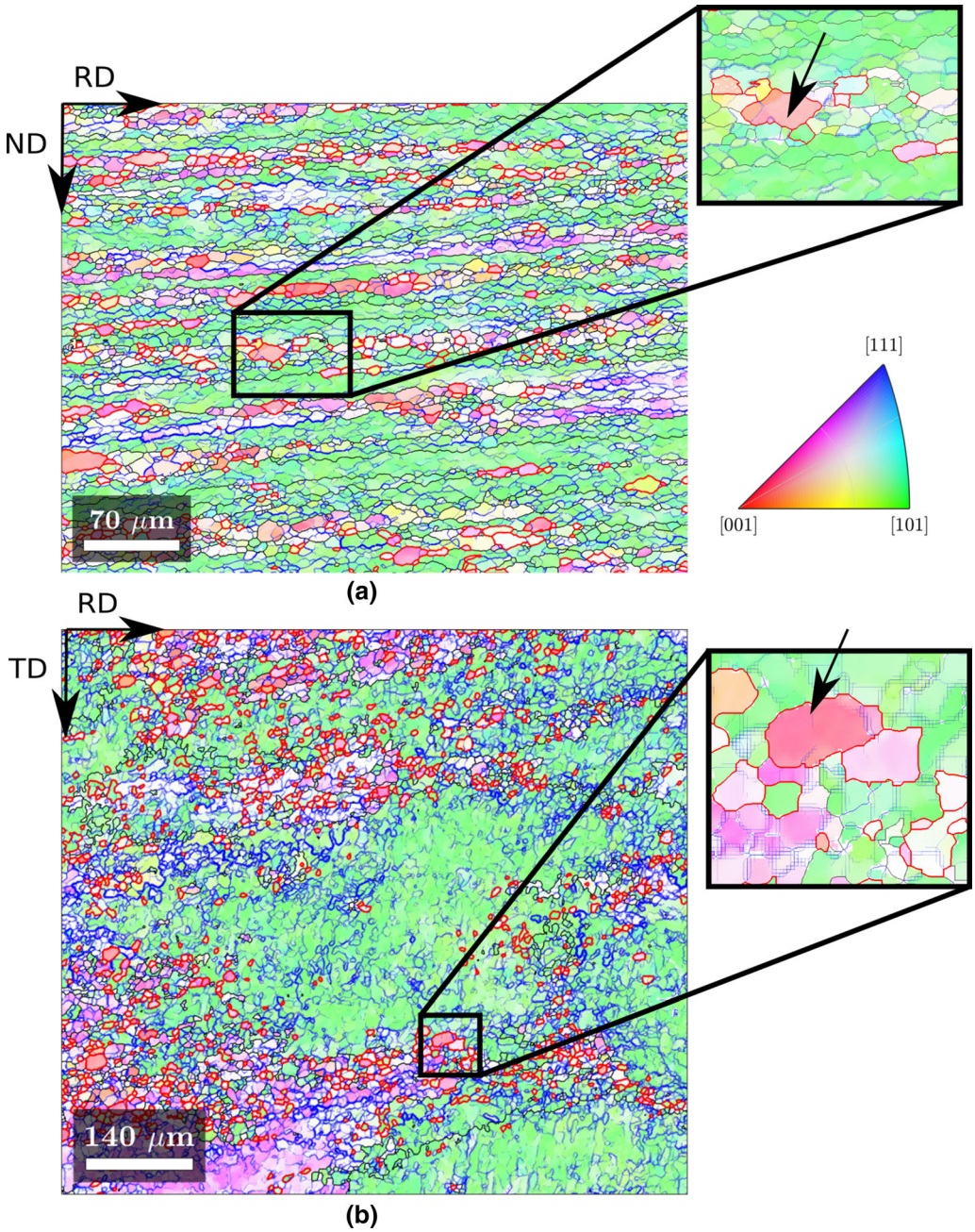

Fig. 7—Microstructure quenched right after deformation: (*a*) EBSD orientation map in the RD–ND plane. Measurement step size is 0.4 μm. (*b*) EBSD orientation map in the RD–TD plane. Measurement step size is 1 μm. In (*a*) and (*b*), the high angle boundaries of recrystallized grains are plotted in red lines. The high angle boundaries (θ higher than 10 deg) of deformed grains are plotted in black lines. The low angle boundaries (θ between 1 and 10 deg) are plotted in blue lines. The color code defined on the standard triangle refers to the normal direction (Color figure online).

2. *Contribution of stored energy in the development of coarse recrystallized grains*

The local variations in stored energy are estimated through $\left|\overline{KAM}_{neighbor} - \mathrm{GAM}_{rex}\right|$ values as mentioned in SectionII–F and their contribution in the preferential growth of "near Cube" oriented grains is investigated as shown in Figure 14. The mean $\left|\overline{KAM}_{neighbor} - GAM_{rex}\right|$ values for both "near Cube" and other orientations (shown by the red lines) are almost similar in the microstructure right after deformation, meaning that the accumulation of stored energy is almost similar for the close neighborhood of "near Cube" and other-oriented recrystallized grains. This suggests that particular local stored energy gradients do not seem to promote the growth of "near Cube" oriented recrystallized grains in the early stages of recrystallization. This is consistent with the poor size advantage shown in Section III–D–1.

The role of stored energy in boundary migration during post-deformation annealing could be further investigated thanks to the sequential annealing

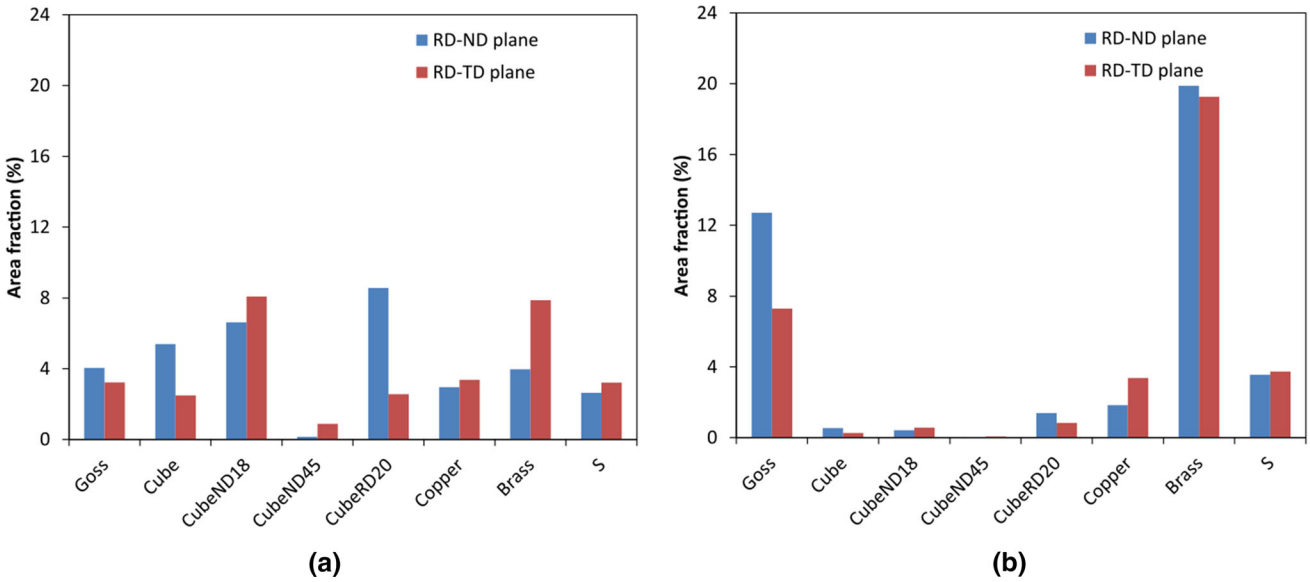

Fig. 8—Area fraction of (*a*) recrystallized and (*b*) deformed grains belonging to the typical texture components in aluminum alloys.

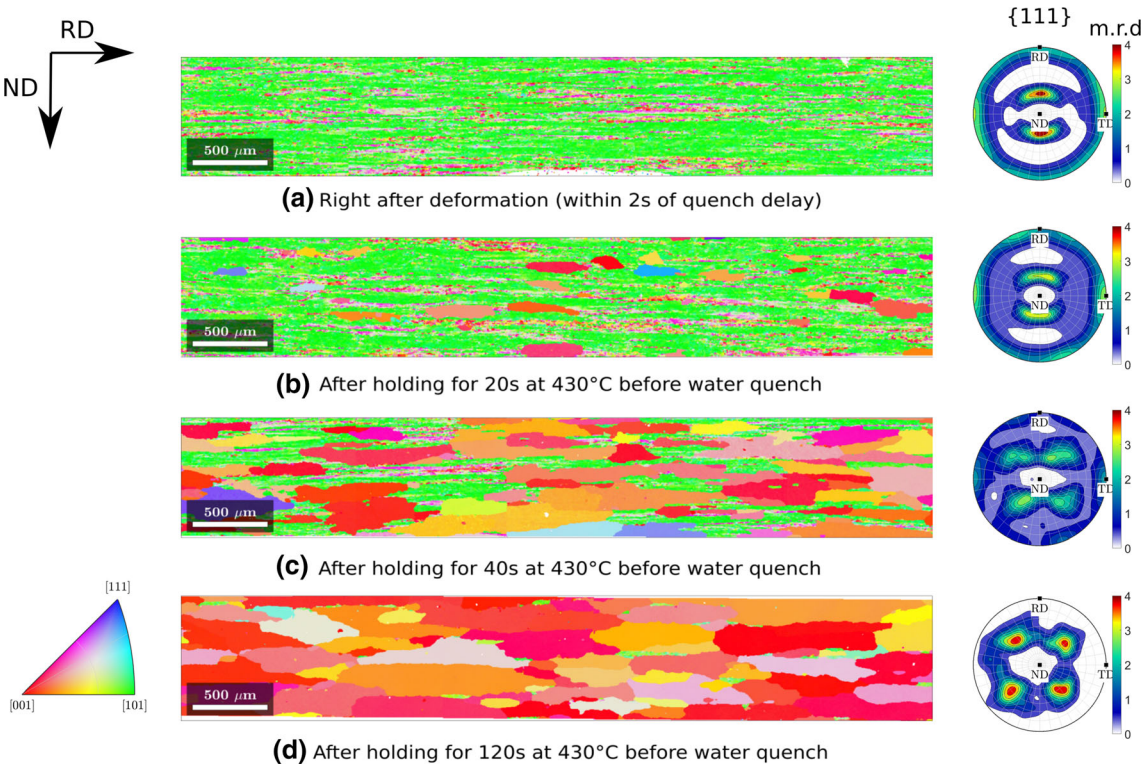

Fig. 9—(*a–d*) EBSD orientation maps showing microstructure evolution during holding at 430 °C after deformation. The color code defined on the standard triangle refers to the normal direction. The measurement step size is 3 μm. {111} pole figure corresponding to each EBSD orientation map is shown on the right (Color figure online).

experiments. It is clear that grain overgrowth is stopped when coarse recrystallized grains impinge on each other and that coarse recrystallized grains contain some stable island grains (see Figures 10 and 15). Therefore, grain boundaries can be classified into two types: moving and non-moving boundaries. The moving boundaries consist of the boundaries between coarse recrystallized grains and deformed ones (blue colored in Figure 15). In contrast, the non-moving boundaries are composed of boundaries between impinged coarse recrystallized grains (brown-colored in Figure 15), boundaries between island grains and coarse

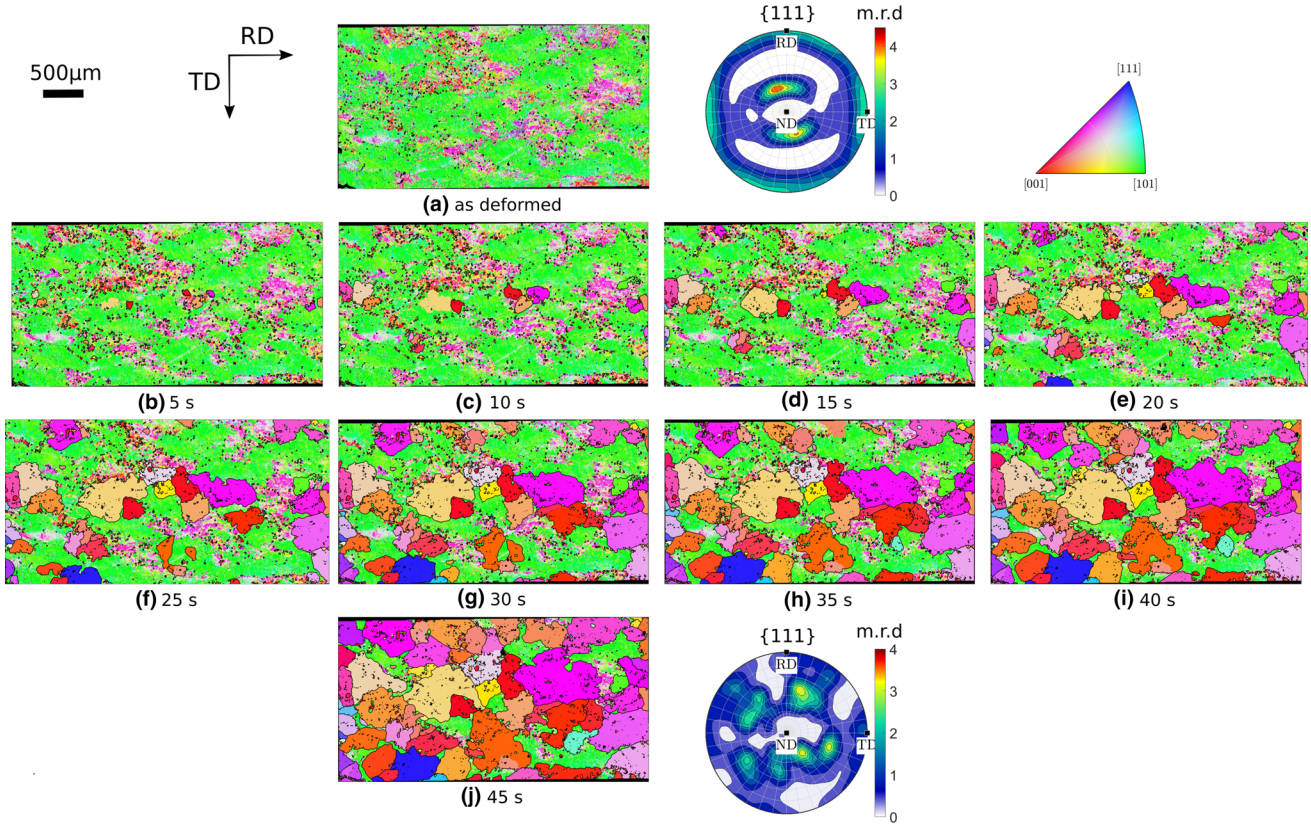

Fig. 10—(*a–j*) EBSD orientation maps showing microstructure evolution during successive annealing steps using a fast heating stage coupled to SEM. The boundaries of recrystallized grains are plotted in black. The color coding defined in the standard triangle refers to ND. The measurement step size is 3 μm. {111} pole figures of the initial and final states are shown in (*a*) and (*j*), respectively. The recrystallized grains are less elongated than in Fig. 9 as the plane of observation is different (Color figure online).

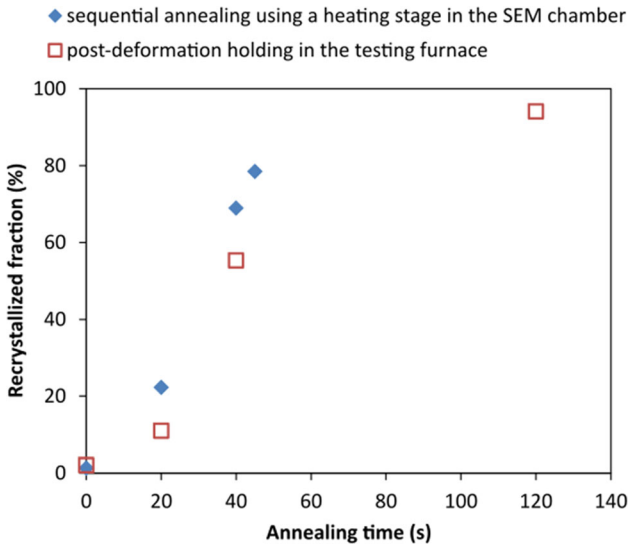

Fig. 11—Comparison of recrystallization kinetics between post-deformation holding in the testing furnace and sequential annealing using a heating stage in the SEM chamber.

recrystallized ones (green colored in Figure 15), and boundaries between small recrystallized grains and deformed ones (black colored in Figure 15).

In this way, moving and non-moving boundaries are determined in each EBSD orientation map (shown in Figure 10), and the local variations in stored energy are estimated by calculating the $\overline{KAM}_{neighbor} - GAM_{Rex}$ values across these boundaries during different steps of sequential annealing. The results of these calculations are illustrated in Figure 16.

It is evident from Figure 16(a) that the difference in stored energy between deformed matrix and coarse recrystallized grains is positive and increases during sequential annealing, meaning an increase in the driving pressure between coarse recrystallized grains and deformed matrix. This suggests that, as they migrate, the boundaries of the coarse recrystallized grains meet deformed matrix areas with higher stored energy levels. This confirms the role played by the stored energy in the migration of the boundaries between coarse recrystallized grains and deformed matrix.

For boundaries between deformed matrix and small recrystallized grains (see Figure 16(c)), the number fraction of boundaries having a $\overline{KAM}_{neighbor} - GAM_{Small}$ between 0.5 and 1 deg increases, while the number fraction of boundaries having a $\overline{KAM}_{neighbor} - GAM_{Small}$ higher than 1 deg decreases. This means that the difference in stored energy across boundaries between small grains and deformed matrix decreases during sequential annealing steps, suggesting that the

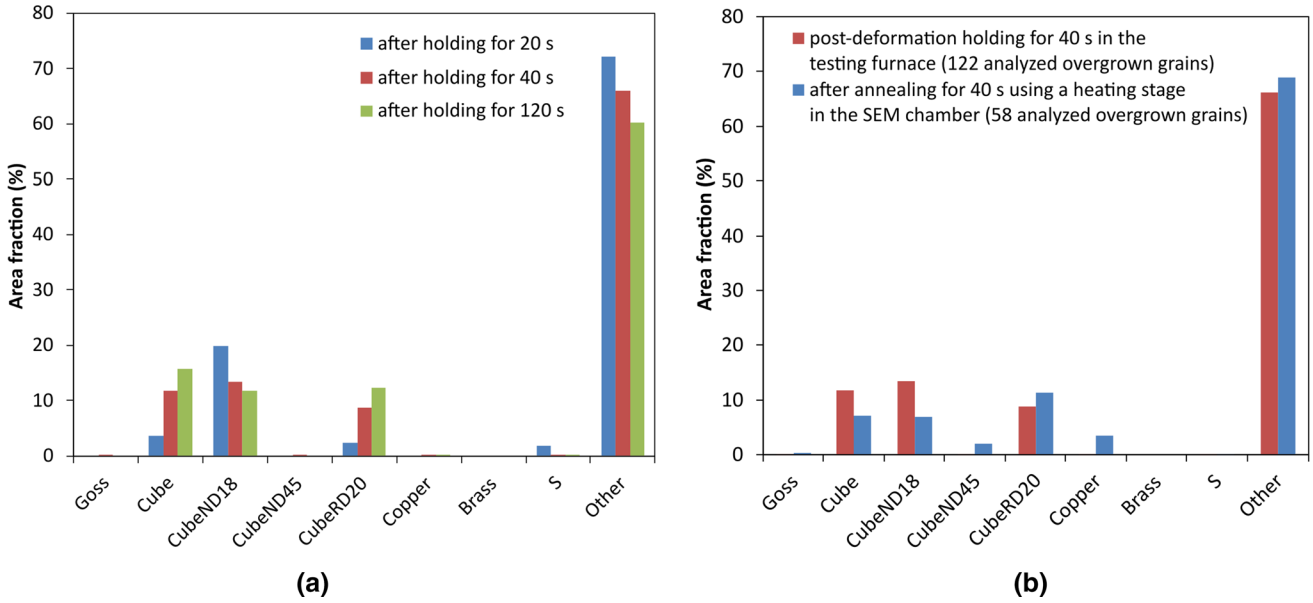

Fig. 12—(*a*) Evolution of texture of coarse recrystallized grains during post-deformation holding, (*b*) Comparison of orientation of coarse recrystallized grains observed after 40 s between post-deformation holding in the testing furnace and sequential annealing in the SEM chamber.

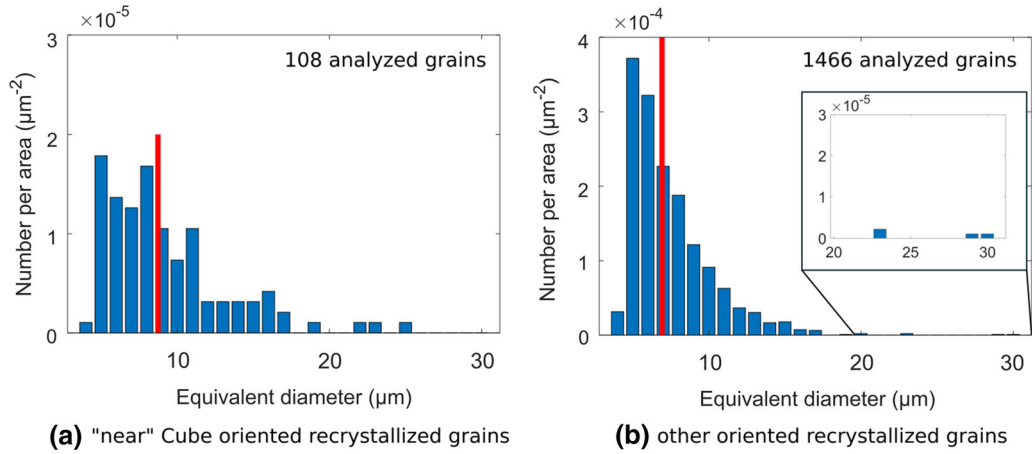

Fig. 13—Size distribution for (*a*) "near Cube" and (*b*) other-oriented recrystallized grains examined right after deformation in the RD–ND plane. The number per area is calculated as the number of recrystallized grains divided by the EBSD orientation map area. Red lines show the average value of the distributions. The analyzed area is 1.13 mm × 0.84 mm (Color figure online).

deformed grains surrounding small recrystallized grains are reducing their stored energy by recovery or that small recrystallized grains grow slightly by consuming the stored energy in their initial close neighborhood and then stop growing. Figure 17 shows the evolution of grain boundaries during different sequential annealing steps. The boundaries between small recrystallized grains and deformed matrix are plotted in black lines, whereas the boundaries of coarse recrystallized grains are plotted in red lines. It is clear from Figure 17(a) that the number of recrystallized grains decreases from one annealing step to another because small recrystallized grains are consumed by coarse recrystallized grains that are growing, leading to their complete disappearance or to their transformation into island grains (represented by blue lines in Figure 17) as indicated by the green arrow on Figure 17(b). The decrease in the number fraction of boundaries between small recrystallized grains and deformed ones for $\overline{KAM}_{neighbor} - GAM_{Small}$ values higher than 1 deg (see Figure 16(c)) suggests that the small recrystallized grains having higher stored energy gradients across their boundaries tend to disappear, while the small recrystallized grains having lower stored energy gradients across their boundaries remain stable. Figure 17(b) shows zooms onto the maps shown by Figure 17. It is evident from Figure 17(b) that the size of small recrystallized grains before their disappearance does not seem to increase with annealing time. Therefore, the recovery of the deformed areas surrounding small recrystallized grains could be also behind the decrease in the driving force for the migration of these boundaries, which is consistent with their stagnation.

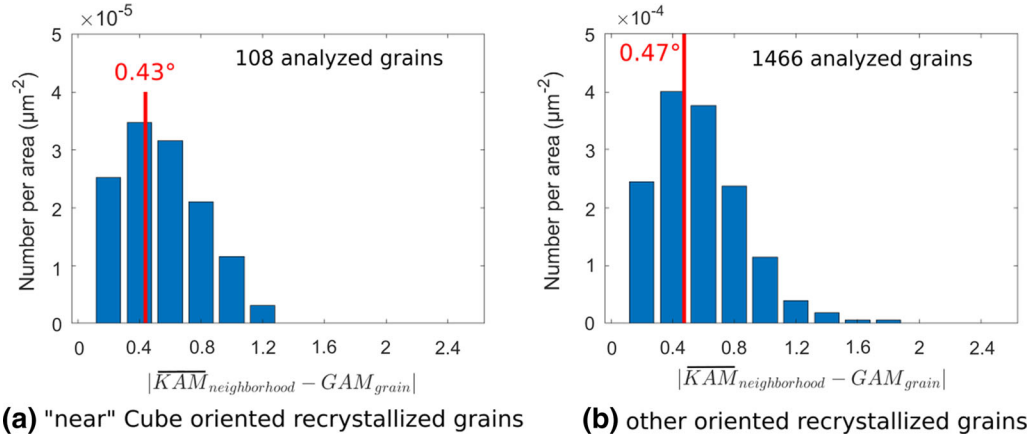

Fig. 14—$\left|\overline{KAM}_{neighbor} - GAM_{rex}\right|$ distribution for (*a*) "near Cube" and (*b*) other-oriented recrystallized grains. The number per area is calculated as the number of recrystallized grains divided by the EBSD orientation map area. The red lines show the average value of the distributions. The analyzed area is 1.13 × 0.84 mm. The EBSD measurement step size is 1 µm (Color figure online).

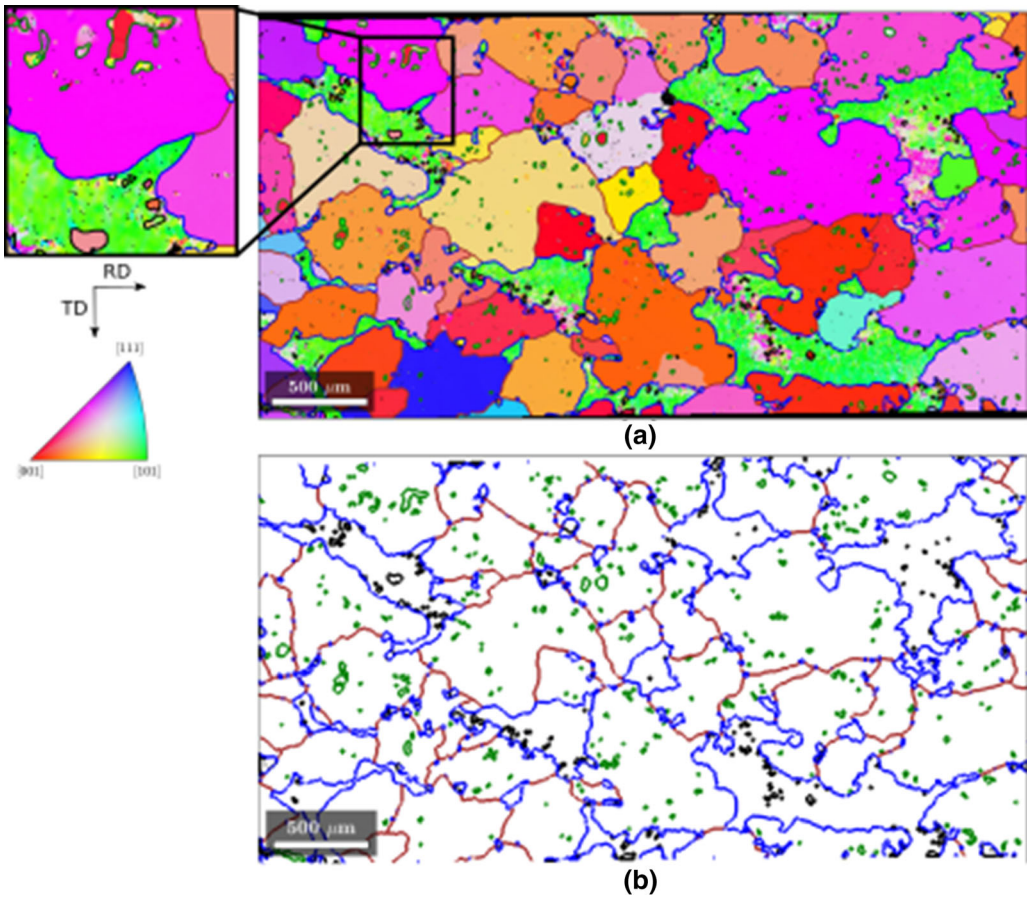

Fig. 15—(*a*) EBSD orientation map of the final state obtained during sequential annealing showing boundaries between coarse recrystallized grains and deformed ones in blue, boundaries between impinged coarse recrystallized grains in brown, boundaries between island grains and coarse recrystallized ones in green, and boundaries between small recrystallized grains and deformed ones in black. The zoom into a randomly chosen area in the observed region shows different types of grain boundaries. The color coding as illustrated by the standard triangle is defined according to the normal direction. The EBSD measurement step is 3 µm. (*b*) Same color coding of grain boundaries only (Color figure online).

For boundaries between coarse recrystallized grains (see Figure 16(d)), most of boundaries have a $\overline{KAM}_{neighbor} - GAM_{Coarse}$ between 0.5 and 1 deg, meaning that the difference in stored energy between coarse recrystallized grains once they are in contact is very low. This result confirms that the absence of difference in stored energy between coarse recrystallized grains explains their stagnation once they are impinged on one another.

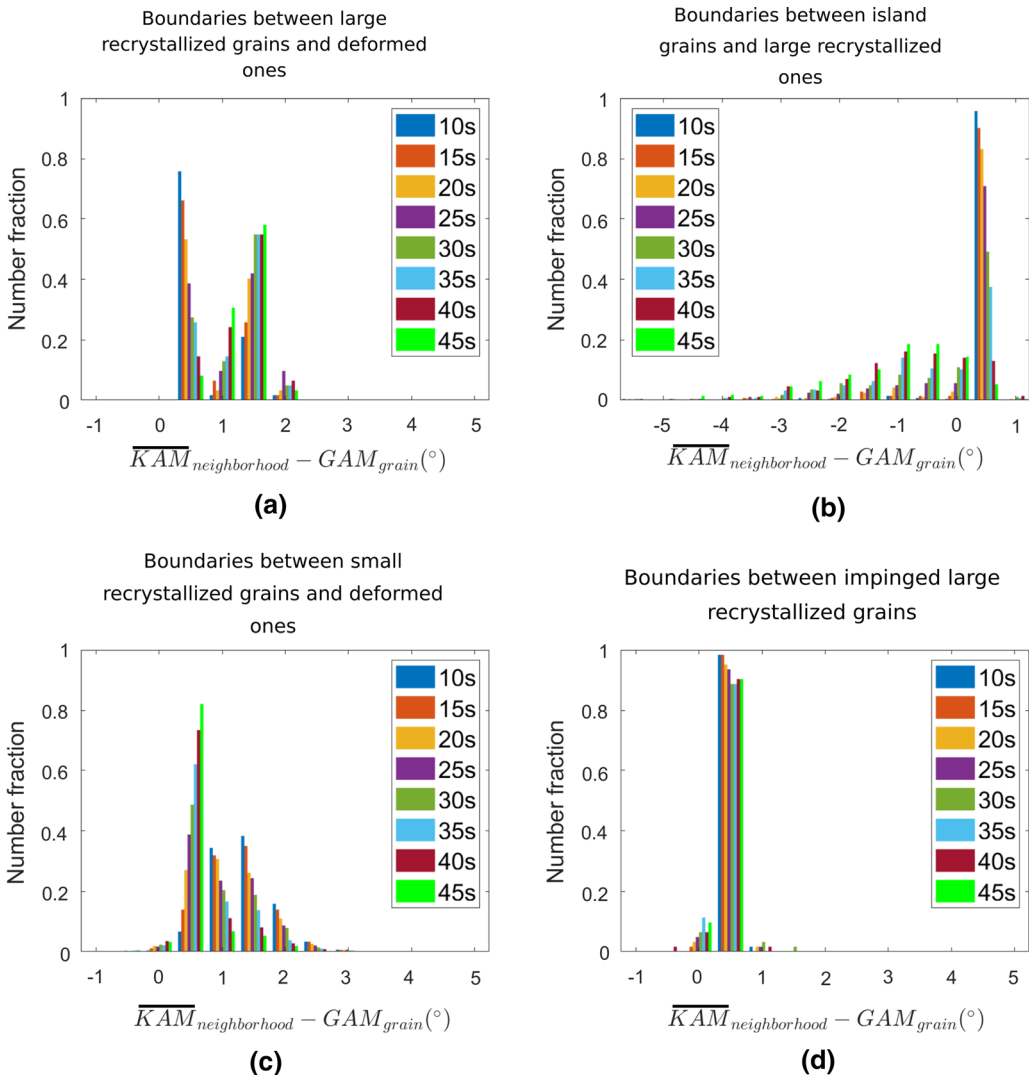

Fig. 16—$\overline{KAM} - GAM$ distribution for boundaries (*a*) between coarse recrystallized grains and deformed matrix, (*b*) between island grains and coarse recrystallized ones, (*c*) between small recrystallized grains and deformed matrix and (*d*) between impinged coarse recrystallized grains.

Finally, for boundaries of island grains (see Figure 16 (b)), the number fraction of boundaries having $\overline{KAM}_{neighbor} - GAM_{island}$ between 0.5 and 1 deg is decreasing whereas the number fraction of boundaries having $\overline{KAM}_{neighbor} - GAM_{island}$ lower than 0.5 deg (including negative values) is increasing during sequential annealing. Figure 17(b) shows clearly that the number of island grains increases with annealing time. These island grains may originate from small recrystallized grains that are formed right after deformation (see green arrow on Figure 17(b)) or from subgrains present in deformed grains as can be seen by Figures 18(a) and (b). The increase in the number fraction of boundaries of island grains having negative $\overline{KAM}_{neighbor} - GAM_{island}$ values accompanied by a decrease in the number of boundaries of island grains having $\overline{KAM}_{neighbor} - GAM_{island}$ between 0.5 and 1 deg could be explained by the increase in the number of island grains made of subgrains with annealing time. The stored energy inside coarse recrystallized grains is therefore lower than the stored energy inside island grains made of subgrains. Despite this, the boundaries of these island grains remain immobile [as can be seen by Figures 17 and 18(a) and (b)], suggesting that the stored energy is not responsible for the occurrence of island grains and that another parameter must be responsible for this.

BSE images showing qualitatively the distribution of precipitates around some island grains [see Figures 18(c) and (d)] suggest that precipitates located at the boundaries of island grains cannot be held entirely responsible for their stagnation either. In fact, the amount of precipitates inside and around island grains seem to be qualitatively similar from these BSE images. Additionally, the precipitates observed around the island grain shown by a black box on Figure 18(c) suggest that boundaries of this grain were able to break away from the surrounding precipitates to reach the following position after annealing. This clearly indicates that the boundaries of stable island grains are not strongly affected by second-phase particles pinning. The

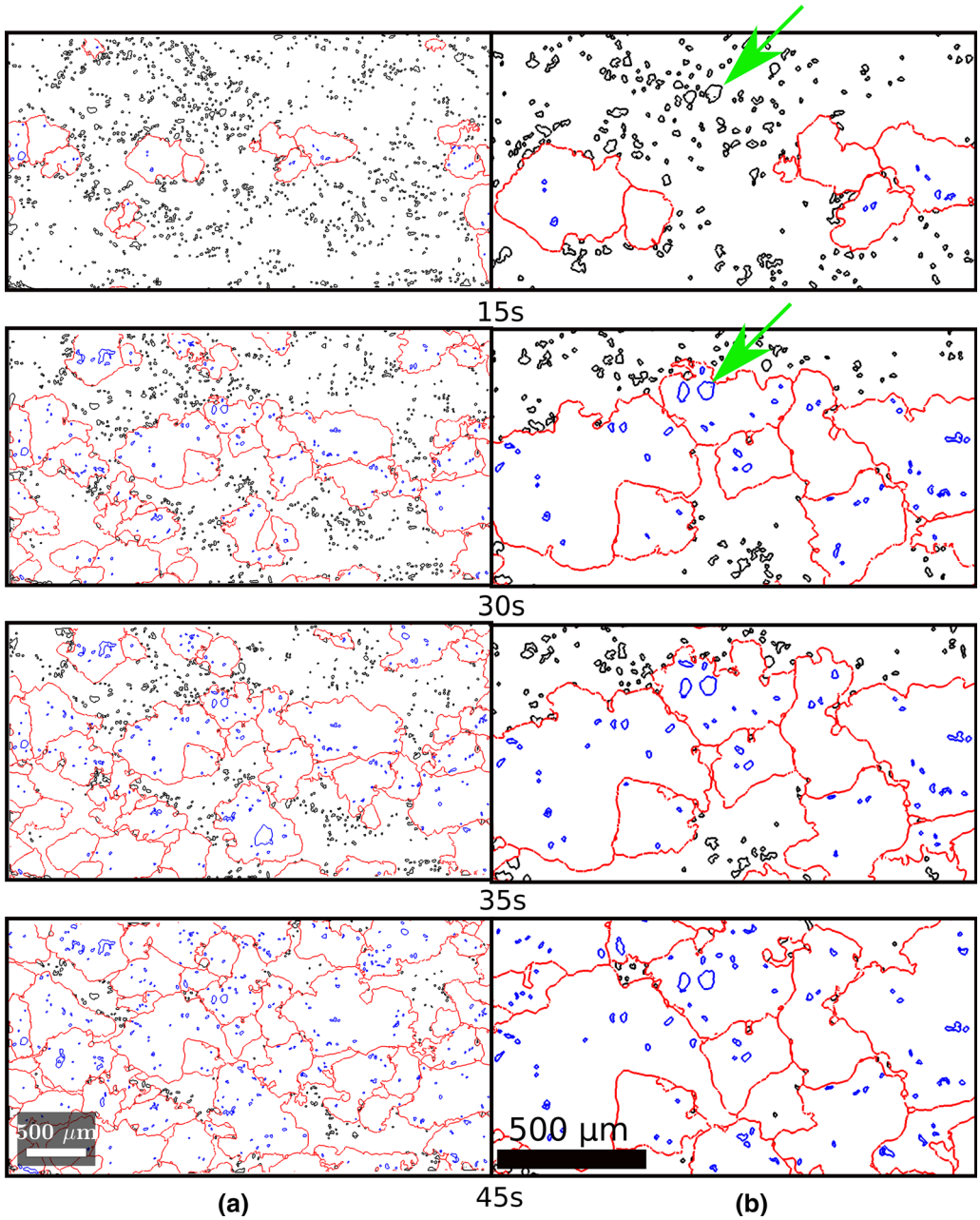

Fig. 17—(*a*) Evolution of grain boundaries during different sequential annealing steps. (*b*) Zoom into each grain boundary map shown in (*a*). Boundaries between small recrystallized grains and deformed ones are plotted by black lines. Boundaries of coarse recrystallized grains are plotted by red lines. Boundaries between island grains and coarse recrystallized ones are plotted by blue lines. The green arrow shows a small recrystallized grain that is transforming into an island grain (Color figure online).

formation of island grains has been attributed to the presence of low mobility or low energy boundaries in many studies.[26,27,49] This will be addressed in "III–D–4" secion.

3. *Influence of second-phase particles*

Despite Smith–Zener pinning, grain overgrowth occurs, suggesting that the driving pressure for the development of coarse recrystallized grains is higher than the pinning pressure. In order to verify this hypothesis, the three driving pressures controlling grain boundary migration are estimated as described in Section II–F. The numerical data used for these calculations are shown in Table III. f_{spp} and d_{spp} are the area fraction and mean equivalent circle diameter of second-phase particles all types included, respectively. R_{rex} is the mean recrystallized grain radius determined in the RD–ND plane right after deformation. The Smith-Zener pinning pressure P_Z and the capillarity pressure P_C are estimated according to Eqs. [6] and [7] (Section II–F), respectively and their estimated values are shown in Table IV.

The driving pressure due to stored energy P_{SE} needs to exceed the sum $|P_Z + P_C|$ (*i.e.*, $\approx$ 150 kPa), so that

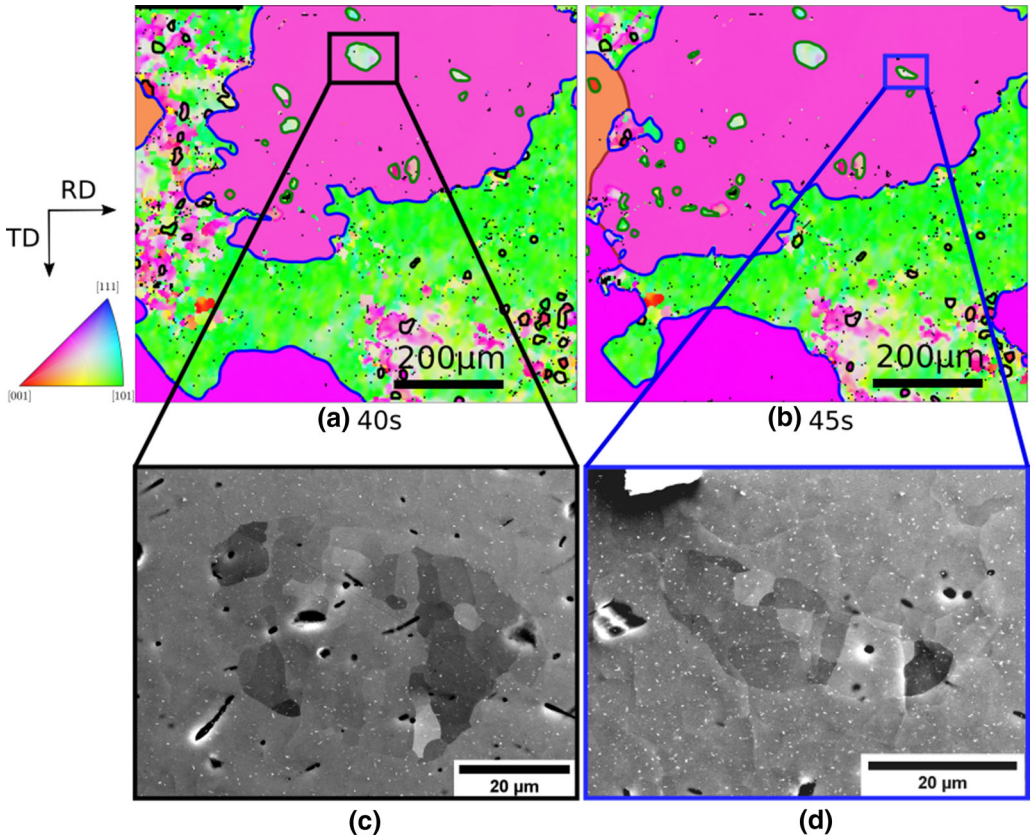

Fig. 18—Formation of stable island grains isolated within coarse recrystallized grains during sequential annealing: (*a*, *b*) Cropped EBSD orientation maps showing boundaries between coarse recrystallized grains and deformed ones in blue, boundaries between impinged coarse recrystallized grains in brown, boundaries between island grains and coarse recrystallized ones in green, and boundaries between small recrystallized grains and deformed ones in black. The color coding as illustrated by the standard triangle is defined according to the normal direction. The EBSD measurement step is 3 μm, (*c*, *d*) BSE images showing the distribution of precipitates around some island grains (shown by black and blue boxes in (a) and (b)) (Color figure online).

Table III. Estimated Values Useful for Driving and Pinning Pressures Calculation

Parameters	2D
f_{spp}(Pct)	1.2
d_{spp}	0.19 μm
R_{rex}	3.6 μm

Table IV. Estimated Driving and Pinning Pressures for the Growth of Recrystallized Grains Observed Right After Deformation

Pressures	Estimated Values (kPa)
P_Z	≈ 60
P_C	≈ 90
P_{SE}	$> \mid P_Z + P_C \mid$

the growth of recrystallized grains formed right after deformation occurs. From Eq. [5] and when x is taken to be equal to the measurement step size (*i.e.*, 1 μm in this case), it can be deduced that the quantity $c^*(\overline{KAM}_{neighbor} - GAM_{rex})$ should be greater than 0.75 deg. If we consider that $c = 1$ (*i.e.*, only the contribution of GNDs is considered), 16 pct of recrystallized grains have $c^*(\overline{KAM}_{neighbor} - GAM_{rex})$ values higher than 0.75 deg (based on Figure 14). The proportion of boundaries of recrystallized grains satisfying $c^*(\overline{KAM}_{neighbor} - GAM_{rex})$ higher than 0.75 deg could be even greater if considering the contribution of SSDs in the stored energy (*i.e.*, $c > 1$). It can be therefore concluded that some recrystallized grains right after deformation can indeed overcome the Smith–Zener pinning pressure exerted by second-phase particles and then grow at the expense of deformed matrix until mutual impingement. This explains the final coarse recrystallized grain size. Nevertheless, the final anisotropic shape of coarse recrystallized grains cannot be explained by Smith–Zener pinning, nor by stored energy differences.

4. *Anisotropic grain growth behavior*

The difference in stored energy between the recrystallized grains and the deformed ones observed in the as-deformed and quenched microstructure seems to be the key factor leading to grain overgrowth. Smith–Zener

pinning pressure can be overcome in the presence of such difference in stored energy. However, these two parameters cannot explain the anisotropic grain growth behavior and the fact that specific orientations ''near Cube'' are more prone to overgrowth.

Role of large Fe containing particles and finer precipitates The shape of coarse recrystallized grains could be due at least partly to the alignment of Fe containing particles. In fact, as clearly visible in the RD–ND plane (see Figure 19(a)), Fe containing particles are aligned with the RD and located mainly on the boundaries of the original grains (see Figure 5), which are flattened due to the high level of deformation ($\varepsilon \approx 2.4$). The pinning effect exerted by these Fe containing particles is expected to be stronger in the ND than in the RD, due to their elongated shape, as can be seen in Figure 20. Nes *et al.*[50] estimated the Smith–Zener pinning force when a grain boundary meets an ellipsoidal particle. Two situations are possible in this case and are presented in Figure 20: case 1 and case 2. The Smith–Zener pinning force exerted by the particle in case 1 is much higher than the one in case 2, leading to a growth disadvantage of coarse recrystallized grains in the ND and therefore to an elongated shape of coarse recrystallized grains in the plane RD–ND. Figure 19(b) provides a hint of the influence of these particles since it clearly shows Fe containing particles located at the horizontal boundaries of a coarse recrystallized grain.

Nevertheless, some Fe containing particles are located inside the coarse recrystallized grains (see Figure 19(b)). This may be the result of a situation similar to case 2 shown in Figure 20, where the vertical boundaries of a coarse recrystallized grain are able to pass through Fe containing particles. Horizontal boundaries breaking away from these Fe containing particles could also explain this observation, but it is less likely as the Smith-Zener pinning is stronger in this configuration.

The inhomogeneous distribution of finer precipitates including Mg_2Si/Si and dispersoids has been reported in the literature[11,51,52] as another possible reason for the elongated shape of coarse recrystallized grains.

Role of orientation pinning Orientation pinning could also be another explanation for the obtained shape of coarse recrystallized grains. Deformed grains right after hot compression are more elongated in the RD–ND plane than in the RD–TD plane (see Figure 7). Recrystallized grains with orientations different than the orientations of deformed grains will preferentially grow at the expense of deformed grains.[11,24] Due to the elongated shape of deformed grains in the RD–ND plane, recrystallized grains have a higher probability to meet a disfavourable orientation in the ND than the RD, resulting in a growth advantage of coarse recrystallized grains in the RD than in the ND.

The comparison between the shape of coarse recrystallized grains in the RD–ND plane and RD–TD plane is therefore consistent with a combined effect of Fe containing particles, possible inhomogeneous distribution of finer precipitates and orientation pinning in the development of such grain shape, or with being controlled by either one or two of these three factors.

Role of misorientation The anisotropic post-dynamic development of coarse recrystallized grains is very

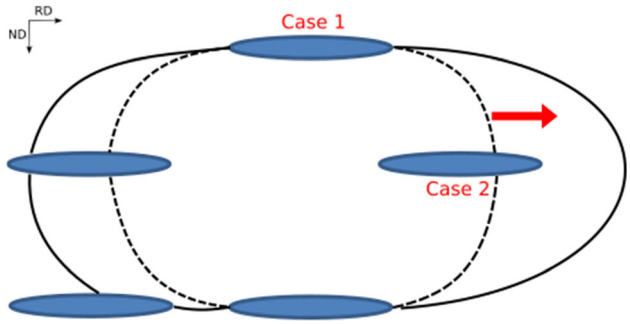

Fig. 20—Schematic illustration of how grain boundaries evolve in the presence of elongated and aligned Fe containing particles.

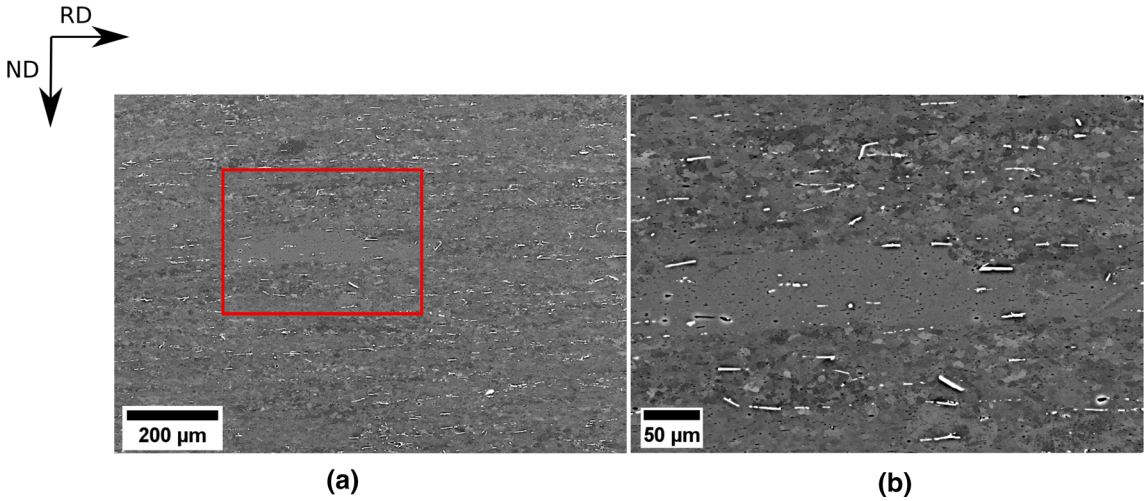

Fig. 19—(*a*) A low magnification SEM BSE image showing the alignment of Fe containing particles with the rolling direction, (*b*) A magnified SEM BSE image of the area pointed out by a red box in (a) showing an elongated coarse recrystallized grain surrounded by Fe containing particles (Color figure online).

evident from their elongated shape when they are examined in the plane RD–ND (see Figure 9(d)). Nevertheless, it is more subtle when the RD–TD section is examined (see Figure 10(j)). Higher magnification EBSD maps with a smaller measurement step size showing the evolution of another region of interest during sequential annealing in the SEM chamber shed light upon the anisotropic grain growth in the RD–TD

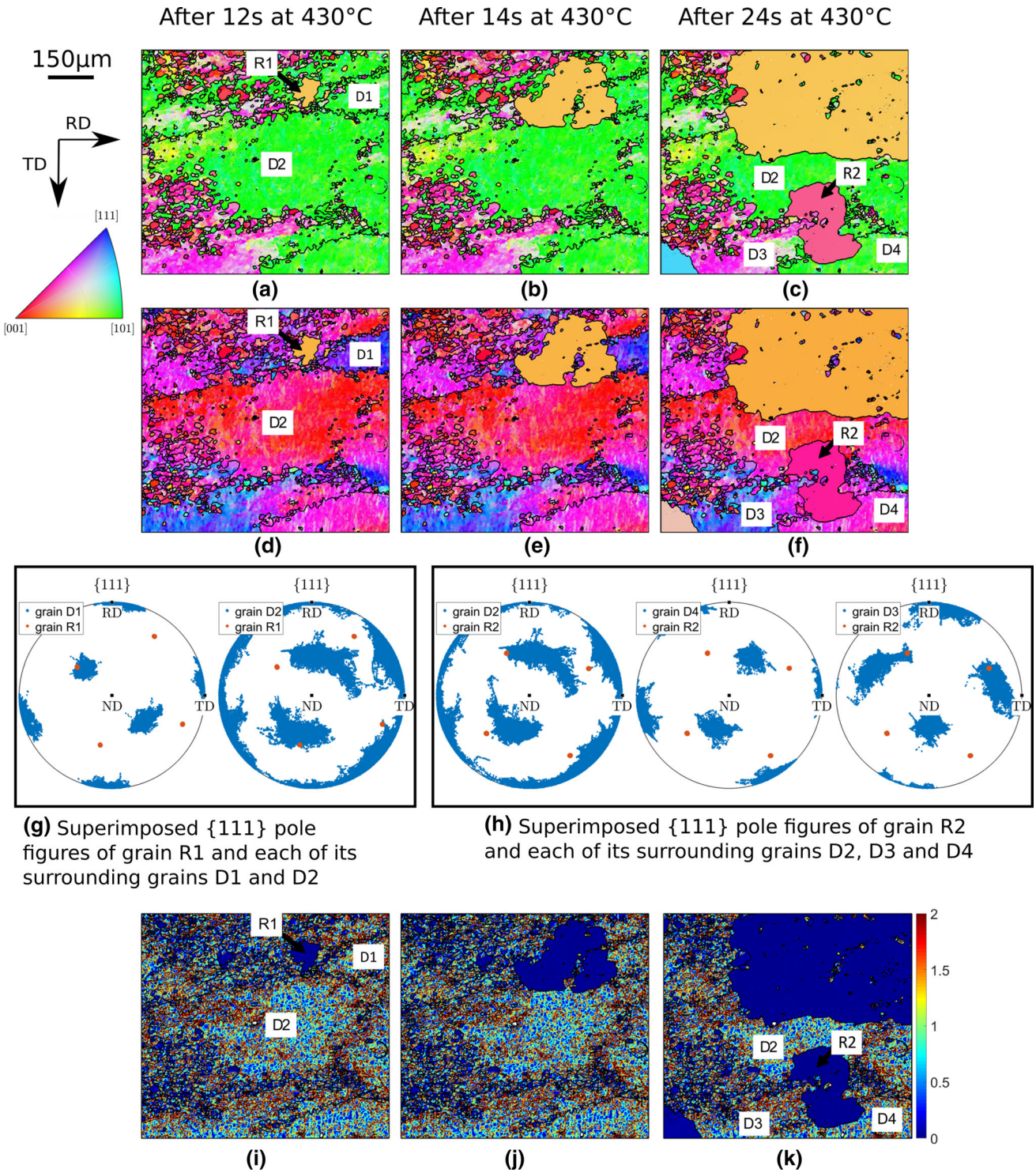

Fig. 21—(*a–f*) Higher magnification EBSD orientation maps with a smaller measurement step size (1 μm) showing the evolution of the microstructure of another region of interest on the hot deformed and quenched sample during sequential annealing in the SEM chamber. The grain boundaries are plotted in black. The color coding is defined according to the standard triangle. (a–c) ND is projected on the standard triangle). (d–f) RD is projected on the standard triangle. (*g–h*) Superimposed {111} pole figures of coarse recrystallized grains R1 and R2 and their surrounding grains. (*i–k*) Corresponding KAM maps (Color figure online).

section as can be seen in Figure 21. The recrystallized grain R1 develops more in the deformed grain D1 than in the deformed grain D2, leading to an elongated shape in the RD. However, the recrystallized grain R2 develops more in the deformed grains D2 and D4 than in the deformed grain D3 although D3 has higher KAM values and therefore stored energy than D2 and D4 (see Figure 21(k)). Even though those observations can be biased by 2D sectioning effect (*i.e.* the migration rate normal to the grain boundary plane is unknown as the grain boundary inclination itself is unkown), these suggest that the growth speed is influenced by the misorientation between the recrystallized grain and its neighboring environment.

The misorientations at moving and non-moving boundaries during different steps of the annealing sequence are calculated and compared to investigate the possible effect of misorientation on boundary migration. Actually, both the correlated and uncorrelated misorientations are calculated. The correlated misorientation is calculated from the orientations of neighboring pixels located on each side of the boundary. On the other hand, the uncorrelated misorientation is calculated assuming no spatial correlation between the pixels. In other words, at the boundaries between coarse recrystallized grains and deformed ones, the uncorrelated misorientation is calculated between pairs of pixels, where the first pixel is randomly selected from the coarse recrystallized grains and the second pixel is randomly selected from the deformed grains in the whole map. At the boundaries between impinged coarse recrystallized grains, the first and second pixels are randomly selected from coarse recrystallized grains in the whole map. At the boundaries between island grains and coarse recrystallized ones, the first pixel is randomly selected inside island grains whereas the second pixel is randomly selected from coarse recrystallized grains in the whole map. At the boundaries between small recrystallized grains and deformed ones, the first pixel is randomly selected from small recrystallized grains and the second pixel is randomly selected from deformed grains in the whole map.

If the correlated and uncorrelated misorientation distributions are different, this indicates that the spatial arrangement of the grains is not random and that there are special boundaries that are favored between grains (*e.g.*, boundaries having a low energy as discussed in Reference 53). On the other hand, if the correlated and uncorrelated misorientation distributions are similar, this means that there is a random spatial arrangement of the grains and that the misorientation distribution is just the result of the crystallographic texture.[54]

The correlated and uncorrelated misorientation angle distributions for different types of boundaries during different annealing steps are shown in Figure 22. It is clear that the correlated and uncorrelated misorientation angle distributions are very different for all types of boundaries except for the boundaries between coarse recrystallized grains. Provided that statistics are good enough, this means that the probability for the occurrence of a certain misorientation between two neighboring grains is not fully determined by the crystallographic texture, but, by another factor that favors specific misorientations.

More specifically, for boundaries between coarse recrystallized grains and deformed ones, the number of pairs of neighboring pixels having a misorientation angle higher than 40 deg increases more during annealing than the number of pairs of neighboring pixels having a misorientation angle lower than 40 deg (see Figure 22(a)). The highest increase in the number of pairs of neighboring pixels is observed for 50–55 deg misorientation angles. This may lead to believe that 50–55 deg boundaries have a fast migration rate as they are involved in the formation of coarse recrystallized grains. Unfortunately, this is not necessarily true since fast moving boundaries tend to disappear as recrystallization progresses. In fact, a fast moving boundary continues moving until meeting another grain with which it forms a slow moving boundary. The remaining grain boundaries are thus more likely to be low mobility boundaries. The remaining grain boundaries may also be thermodynamically favored (*i.e.,* have low energy).[55]

The evolution of correlated misorientation axis distribution corresponding to the 50–55 deg misorientation angles for these boundaries during different sequential annealing steps (Figure 23(a)) shows that the 50–55 deg boundaries between coarse recrystallized grains and the deformed ones have mostly rotation axes near ⟨111⟩ and ⟨101⟩. It is interesting to note that the strength of ⟨111⟩ axis decreases from 10 to 15 seconds and that the strength of ⟨101⟩ axis becomes the highest at the end of sequential annealing (*i.e.,* after 45 seconds) from Figure 23(a). This suggests that the moving boundaries at an early annealing stage have mostly a misorientation of 50–55 deg ⟨111⟩ and that at a later annealing stage, either these moving boundaries are slowly modifying their misorientation axis towards ⟨101⟩ as they migrate through orientation gradients of the neighboring deformed grain or new moving boundaries having a misorientation axis close to ⟨101⟩ form as they meet another deformed grain. It is worth noticing here that since a condition of having a misorientation angle between 50 and 55 deg has been applied in the present analysis, the different annealing steps do not necessarily include the same grain boundary segments. Indeed, the misorientation angle at the recrystallization front is very likely to vary as the boundary moves into orientation gradients. Thus, it is impossible to track the boundaries back in the EBSD maps to get to know which of these two explanations is the best one.

For boundaries between small recrystallized grains and deformed matrix (*i.e.,* non-moving boundaries), the correlated misorientation angle distribution does not show any remarkable maximum during the different annealing steps (see Figure 22(b)). Additionally, the number of pairs of neighboring pixels whatever the misorientation angle between them is decreasing because small recrystallized grains are either consumed by coarse recrystallized grains or becoming themselves coarse recrystallized grains. It is important to note that some small recrystallized grains have 50–55 deg misorientation angles (Figure 22(b)) even after 45 seconds of sequential annealing. The misorientation axis

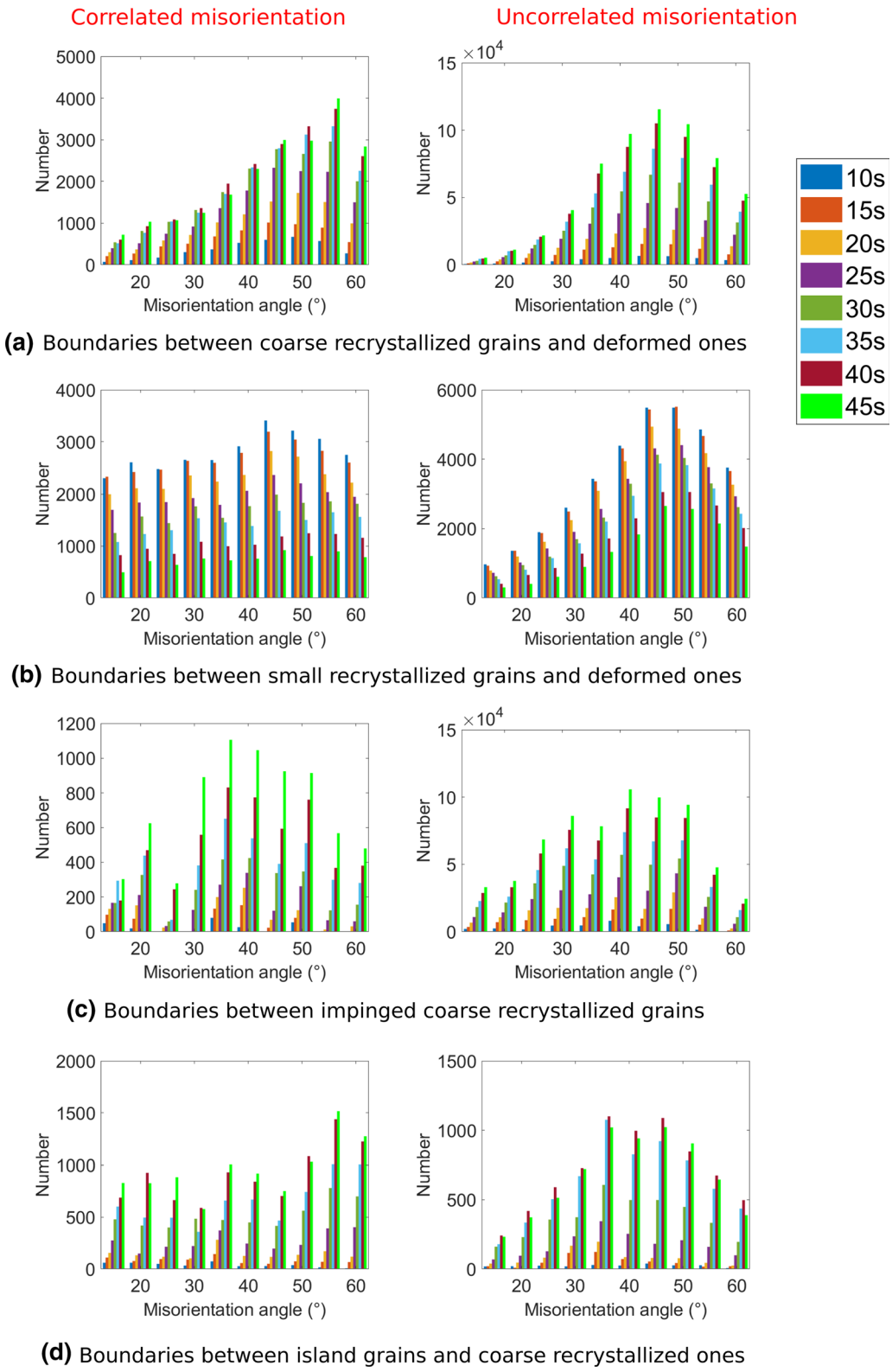

Fig. 22—Correlated (left) and uncorrelated (right) misorientation angle distributions for boundaries: (*a*) between coarse recrystallized grains and deformed matrix, (*b*) between small recrystallized grains and deformed matrix, (*c*) between impinged coarse recrystallized grains and (*d*) between island grains and coarse recrystallized grains. For correlated misorientation, the number corresponds to the number of pairs of neighboring pixels along the grain boundary segments of each type in the map. For uncorrelated misorientation, the number corresponds to the number of pairs of random pixels.

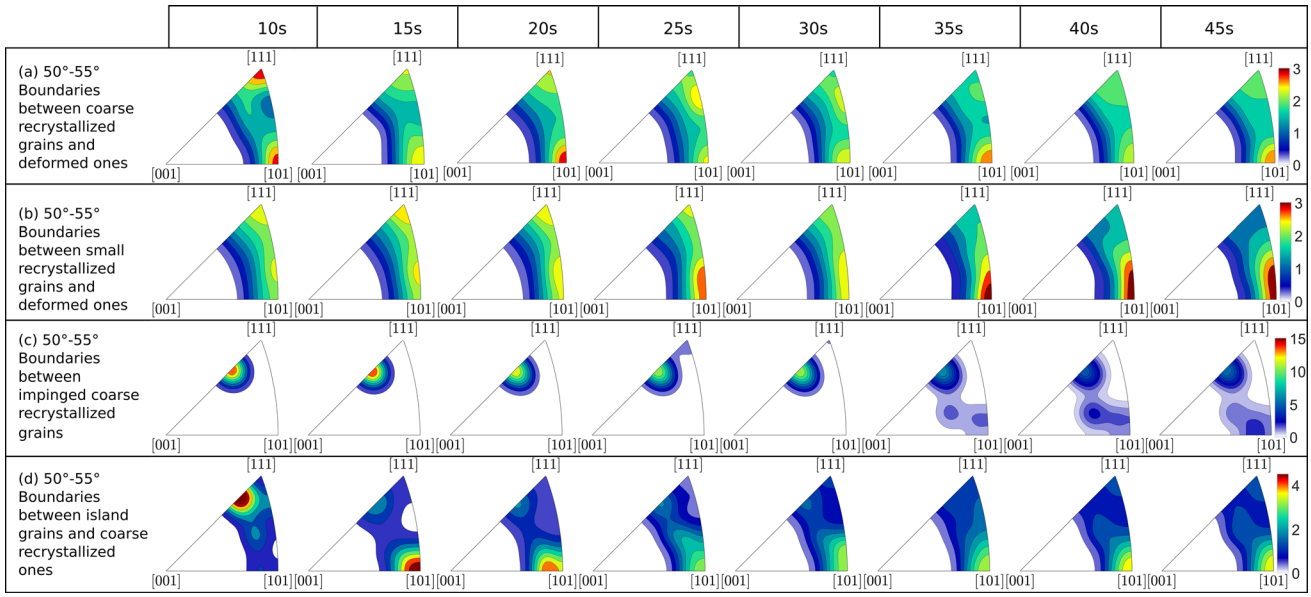

Fig. 23—Evolution of correlated axis distribution corresponding to 50–55 deg misorientation angles during different sequential annealing steps for boundaries: (*a*) between coarse recrystallized grains and deformed matrix, (*b*) between small recrystallized grains and deformed matrix, (*c*) between impinged coarse recrystallized grains and (*d*) between island grains and coarse recrystallized ones.

distributions corresponding to these 50–55 deg misorientation angles during different annealing steps (see Figure 23(b)) show that most of the 50–55 deg boundaries between small recrystallized grains and deformed matrix have rotation axes clustered around ⟨101⟩, suggesting thus that 50–55 deg ⟨101⟩ boundaries are immobile. Therefore, it can be deduced that both misorientation angle and axis are not sufficient to determine the mobility of grain boundaries. 50–55 deg ⟨101⟩ boundaries can be mobile in some cases (at the border of the large growing grains) and immobile in others (at the border of the small non growing grains). This is consistent with the study conducted by Zhang *et al.*[56] where it has been shown in pure nickel that, for a given misorientation (*i.e.,* similar misorientation angle and axis) and similar local driving pressure, a boundary segment may move or not.

For boundaries between island grains and coarse recrystallized ones (see Figure 22(d)), the number of pairs of neighboring pixels is increasing regardless the misorientation angle which makes sense during sequential annealing. In fact, as coarse recrystallized grains develop, the probability of forming island grains increases. The highest increase of the number of pairs of neighboring pixels for these boundaries is again observed at 50–55 deg misorientation angles. The misorientation axis distributions corresponding to these misorientation angles during different sequential annealing steps show that the remaining island grains have misorientation axes clustered around ⟨101⟩ (Figure 23(d)). This confirms that 50–55 deg ⟨101⟩ boundaries can be mobile or immobile, depending on other factors (*e.g.,* precipitate content around the boundary and boundary plane.[22,23]) Formation of island grains is a well-known feature for abnormal grain growth and has been reported in aluminum alloys such as in AA3102[5] and AA5052[57] as well as in other materials including tantalum,[58] Fe-3 pct Si steel[59,60] and copper.[61] It occurs when the growth front moves around the island grain, leaving it behind. This is possible when the velocity of the boundary of the island grain is much smaller than those of its neighboring grains. Since the velocity of a grain boundary (V) depends on mobility (M) and boundary energy (γ), a lower velocity suggests either a lower mobility or a lower energy or both. Koo *et al.*[61] found that the boundaries between island grains and surrounding coarse recrystallized grains are low misorientation angle boundaries ($\theta < 10$ deg) in copper. The formation of island grains was therefore attributed to the low boundary energy and mobility of low angle boundaries between island grains and their neighboring grains.[61] According to Figure 22(d), the boundaries between island grains and coarse recrystallized grains are mostly high angle boundaries. Thus, low angle boundaries are not responsible here for the appearance of island grains. Coincidence site lattice (CSL) boundaries have been reported in many studies[5,57–59] as accountable for the formation of island grains. For instance, Li *et al.*[5] found that, in annealed AA3102, island grains tend to have special boundary relationships, such as Σ3, Σ5 and Σ7, with the coarse recrystallized grains where they are entrapped. This is possible probably due to the low mobility and energy of CSL boundaries.[5]

In order to inspect the role of CSL boundaries, the CSL boundaries are determined based on Brandon's criterion.[62] The percentages of CSL boundaries between island grains and coarse recrystallized ones are subsequently compared to those of CSL boundaries between coarse recrystallized grains and deformed ones as can be seen in Figure 24. The percentages of CSL boundaries between island grains and coarse

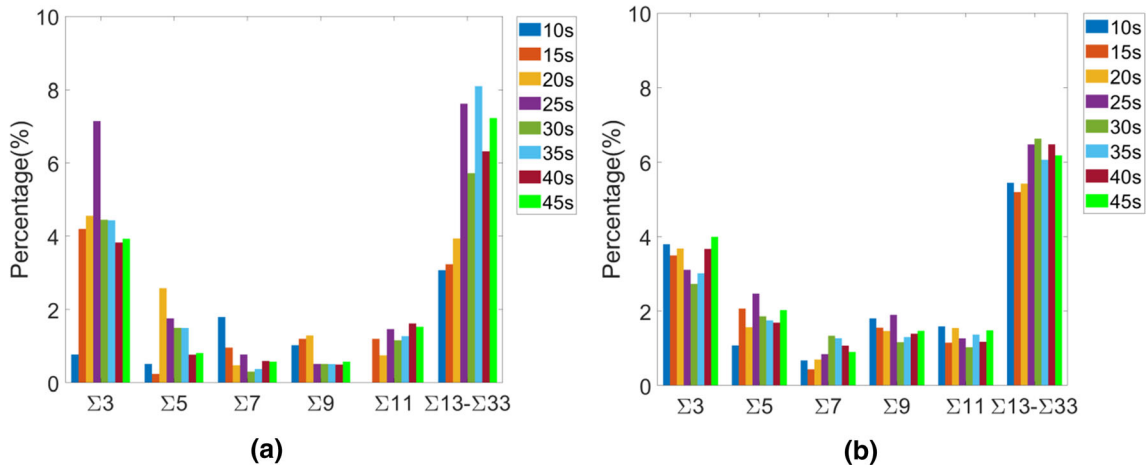

Fig. 24—CSL boundary distributions for (*a*) boundaries between island grains and coarse recrystallized ones and for (*b*) boundaries between coarse recrystallized grains and deformed ones.

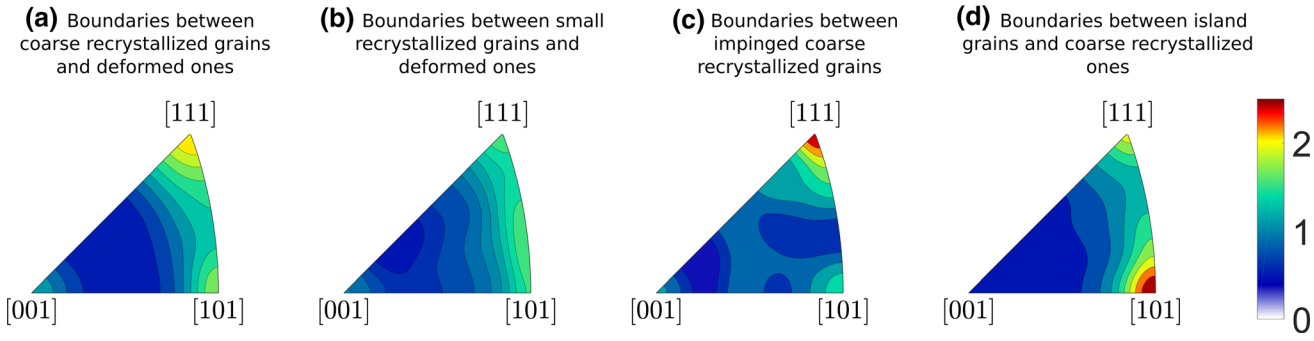

Fig. 25—Correlated misorientation axis distributions for boundaries after the full annealing sequence (45 s): (*a*) between coarse recrystallized grains and deformed matrix, (*b*) between small recrystallized grains and deformed matrix, (*c*) between impinged coarse recrystallized grains and (*d*) between island grains and coarse recrystallized ones.

recrystallized ones and between coarse recrystallized grains and deformed ones are similar, which suggests that CSL boundaries do not play a role of prime importance in the stability of island grains. To conclude, the occurrence of island grains cannot be explained in terms of low angle or CSL boundaries.

This is not totally surprising since the description of boundary energy and mobility as a function of misorientation angle or CSL character does not always apply.[22,23] In addition to misorientation angle, both misorientation axis and boundary plane may play a role in the boundary energy and mobility.[22,23] The effect of misorientation axis on formation of island grains is investigated by plotting the correlated misorientation axis distribution for each grain boundary type as seen in Figure 25. It is clear from Figure 25 that the probability that boundaries between island grains and coarse recrystallized ones have ⟨110⟩ misorientation axes is higher than that of boundaries between coarse recrystallized grains and deformed ones. Both energies and mobilities of 388 distinct grain boundaries in nickel have been calculated using atomic-scale computer simulations by Olmsted *et al.*[22,23] It has been shown that the ⟨101⟩ symmetric tilt boundaries except Σ 11 50.48 deg ⟨101⟩ are high in energy. However, ⟨101⟩ symmetric tilt boundaries have a very wide range of mobilities depending on the misorientation angle and boundary plane. Therefore, the stability of island grains may be due to the low mobility of some particular ⟨101⟩ boundaries. However, this is not a sufficient reason because there as some misorientation angles/axes in common between boundaries between coarse recrystallized grains and deformed ones and those between island grains and coarse recrystallized ones (*e.g.,* 50–55 deg ⟨101⟩, Figure 23). Second-phase particles as shown in Section III–D–1 (see Figure 18) do not seem to explain either the stability of island grains. Therefore, the remaining factors that may explain the stability of these island grains are the boundary plane, the impurity segregation effect or fine precipitation that cannot be resolved with SEM.

Rohrer *et al.*[63] reported that, in FCC materials, the variations in the grain boundary plane orientation contribute more to the energy anisotropy than the variations in the lattice misorientation and that the grain boundary population tends to be inversely correlated to the grain boundary energy.[63] Therefore, it is important to investigate the influence of boundary plane on the

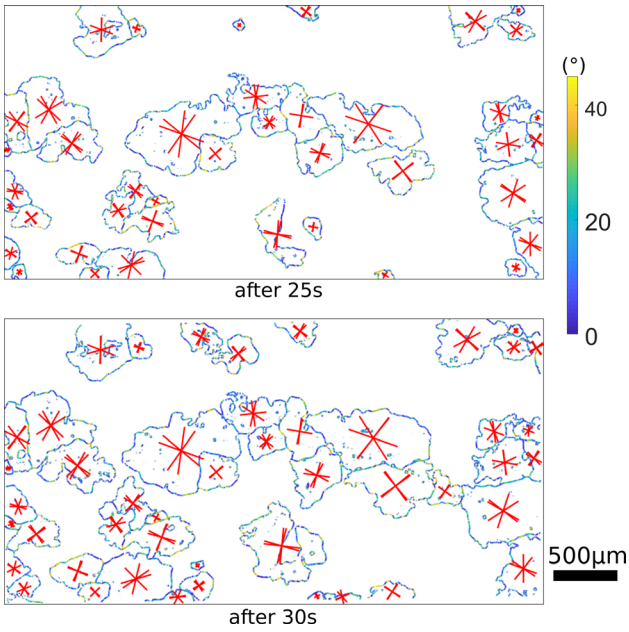

Fig. 26—Grain boundary maps showing the evolution of boundaries of coarse recrystallized grains from 25 to 30 seconds of sequential annealing. The {111} traces within coarse recrystallized grains are plotted in red. All symmetrically equivalent {111} planes are taken into account. The boundaries of coarse recrystallized grains are colored according to the minimum angle between their trace and those of {111} planes (scale bar on the left) (Color figure online).

evolution of the coarse recrystallized grains. The {111} traces corresponding to coarse recrystallized grains are shown by Figure 26. The boundaries of coarse recrystallized grains are also colored according to the minimum angle between their trace and those of {111} planes in Figure 26. It is clear that most of coarse recrystallized grain boundaries are colored in blue, meaning that they are close to {111} traces. This suggests that {111} may play a role in the favorable migration of some boundaries over some others or in the position at which the grain boundary stops or stagnates. Indeed, it has been reported in Reference 64 that grain boundaries migrate in a stop-go manner in a cold rolled pure aluminum (AA1050) single crystal. It has been actually found that the growth of grains occurs by the migration of planar boundary segments (facets) at a constant rate along a direction close to the rolling direction and that the migration of these facets stops at some point during annealing and finally resumes along a different direction.[64] Therefore, the grain boundaries observed between two successive steps during sequential annealing could be in the stop position. The influence of grain boundary plane on the migration rate calls thus for complementary 3D characterization as a perspective of this work.

IV. CONCLUSIONS

The different parameters promoting the overgrowth of recrystallized grains in 6016 aluminum alloy were investigated using hot compression tests followed by both post-deformation holding experiments and sequential annealing in the SEM chamber to follow the evolution of a given region of interest. The evolution of the microstructure was characterized in RD–ND and RD–TD sections by EBSD and the following conclusions were drawn from this work:

- Overgrowth of some recrystallized grains occurs during holding after hot deformation and is clearly visible in both RD–ND and RD–TD sections. Coarse recrystallized grains are elongated in the RD–ND and to a lower extent in the RD–TD plane, suggesting an anisotropic grain development. The coarse recrystallized grains have mostly a "near Cube" orientation with nevertheless a wide scattering;
- "Near Cube" grains have slight initial size advantage among all the small recrystallized grains found in the deformed and quenched state;
- The stored energy seems to promote grain overgrowth. However, it cannot explain for the anisotropic development of coarse recrystallized grains alone;
- For the overgrowing grains, Smith–Zener pinning is overcome by the driving force due to stored energy, leading to growth of these grains at the expense of deformed matrix and most of the other small recrystallized grains until mutual impingement;
- The combined effect of Fe containing particle, possibly inhomogeneous distribution of finer precipitates and orientation pinning is likely to contribute to the development of the anisotropic shape of coarse recrystallized grains. But, these are not the only factors. The influence of the misorientation angle and axis in the anisotropic behavior of coarse recrystallized grains has also been investigated. The analysis of misorientation angle and axis has shown that 50–55 deg ⟨110⟩/⟨111⟩ boundaries are over-represented as compared to the misorientation distribution associated with the actual crystallographic texture. This suggests that 50–55 deg ⟨110⟩/⟨111⟩ boundaries are somehow favored in the microstructure evolution. However, this is not a sufficient condition because other 50–55 deg ⟨110⟩ boundaries were found to be immobile. Many boundaries of coarse recrystallized grains are aligned with or close to {111} plane traces, suggesting that boundary plane may play a significant role in the growth advantage of coarse recrystallized grains and their anisotropic development;
- Although the stored energy provides the driving force for the formation of coarse recrystallized grains, the anisotropic behavior of these grains cannot be explained by stored energy consideration only. This leads to the conclusion that the anisotropic growth is actually due to the combination of multiple factors including alignment of Fe containing particles, heterogeneous distribution of finer precipitates, and the properties (mobility and energy) of the grain boundary types formed between coarse recrystallized grains and their neighbors.

ACKNOWLEDGMENTS

The work received financial support from C-TEC Constellium Technology Center. The authors would like to thank Alain Legendre for conducting hot compression tests, and Bruno Nicolas and Eric Janot for their assistance with the preparation of samples for quantification of precipitates. Suzanne Jacomet and Cyrille Collin are acknowledged for their help with sample preparation and characterization using EBSD. The authors are also very grateful to Dr. Juliette Chevy and Dr. Louis-Marie Rabbe for helpful comments and discussions. Finally, acknowledgements should be given to the DIGIMU consortium partners for fruitful discussions.

CONFLICT OF INTEREST

On behalf of all authors, the corresponding author states that there is no conflict of interest.

REFERENCES

1. O. Engler and J. Hirsch, *Mater. Sci. Eng. A*, 2002, vol. 336, pp. 249–62.
2. O. Engler, C. Schäfer, and H. Brinkman, *Acta Mater.*, 2012, vol. 60, pp. 5217–32.
3. J. Hirsch, *Trans. Nonferrous Metals Soc. China*, 2014, vol. 24, pp. 1995–2002.
4. L. Qin, M. Seefeldt, and P. Van Houtte, *Acta Mater.*, 2015, vol. 84, pp. 215–28.
5. K. Li, T. Zou, D. Li, Y. Peng, D. Shu, *Metall. Mater. Trans. A*, 2019, vol. 50A, pp. 5734–49.
6. N. Lu, J. Kang, N. Senabulya, R. Keinan, N. Gueninchault, and A. Shahani, *Acta Mater.*, 2020, vol. 195, pp. 1–12.
7. J. Dennis, P. Bate, and F. Humphreys, *Acta Mater.*, 2009, vol. 57, pp. 4539–47.
8. H.-C. Kim, C.-G. Kang, M.-Y. Huh, and O. Engler, *Scripta Mater.*, 2007, vol. 57, pp. 325–27.
9. K. Huang, Y.J. Li, and K. Marthinsen, *Mater. Charact.*, 2015, vol. 102, pp. 92–97.
10. K. Huang, O. Engler, Y.J. Li, and K. Marthinsen, *Mater. Sci. Eng. A*, 2015, vol. 628, pp. 216–29.
11. X. Fang, H. Xiao, K. Marthinsen, A. Belyakov, X. Fang, and K. Huang, *Mater. Charact.*, 2020, vol. 166, pp. 110438.
12. V. Miller, A. Johnson, C. Torbet, and T. Pollock, *Metall. Mater. Trans. A.*, 2016, vol. 47A, pp. 1566–74.
13. M. Charpagne, J. Franchet, and N. Bozzolo, *Mater. Design*, 2018, vol. 144, 353–60.
14. X. Wang, Z. Huang, B. Cai, N. Zhou, O. Magdysyuk, Y. Gao, S. Srivatsa, L. Tan, and L. Jiang, *Acta Mater.*, 2019, vol. 168, pp. 287–98.
15. A. Agnoli, M. Bernacki, R. Logé, J.-M. Franchet, J. Laigo, N. Bozzolo, *Metall. Mater. Trans. A*, 2015, vol. 46A, pp. 4405–21.
16. H.-K. Park, J.-H. Kang, C.-S. Park, C.-H. Han, and N.-M. Hwang, *Mater. Sci. Eng. A*, 2011, vol. 528, pp. 3228–31.
17. F. Humphreys and M. Hatherly, 2nd, 2004, p. 658.
18. I. Andersen, O. Grong, and N. Ryum, *Acta Metall. Mater.*, 1995, vol. 43, pp. 2689–2700.
19. P. Rios, *Acta Mater.*, 11997, vol. 45, pp. 1785–89.
20. B. Straumal, W. Gust, L. Dardinier, J. Hoffmann, V. Sursaeva, and L. Shvindlerman, *Mater. Design*, 1997, vol. 18, pp. 293–95.
21. A. Agnoli, M. Bernacki, R. Logé, J.-M. Franchet, J. Laigo, and N. Bozzolo, ed. by Superalloys 2012: The 12th International Symposium on Superalloys.
22. D. Olmsted, E. Holm, and S. Foiles, *Acta Mater.*, 2009, vol. 57, pp. 3704–13.
23. D. Olmsted, S. Foiles, and E. Holm, *Acta Mater.*, 2009, vol. 57, pp. 3694–3703.
24. O. Engler, *Acta Mater.*, 1998, vol. 46, pp. 1555–68.
25. T.-W. Na, H.-K. Park, C.-S. Park, J.-T. Park, and N.-M. Hwang, *Acta Mater.*, 2016, vol. 115, pp. 224–29.
26. K.-J. Ko, P.-R. Cha, D. Srolovitz, and N.-M. Hwang, *Acta Mater.*, 2009, vol. 57, pp. 838–45.
27. D.-K. Lee, B.-J. Lee, K.-J. Ko, and N.-M. Hwang, *Mater. Trans.*, 2009, vol. 50, pp. 2521–25.
28. Y. Huang and F. Humphreys, *Mater. Chem. Phys.*, 2012, vol. 132, pp. 166–74.
29. S. Kim and Y. Park, *Acta Mater.*, 2008, vol. 56, pp. 3739–53.
30. W. Van Geertruyden, H. Browne, W. Misiolek, and P. Wang, *Metall. Mater. Trans. A*, 2005, vol. 36A, pp. 1049–56.
31. A. Eivani, J. Zhou, and J. Duszczyk, *Philos. Magn.*, 2016, vol. 96, pp. 1188–96.
32. Y. Mahmoodkhani, J. Chen, M.A. Wells, W.J. Poole, and N.C. Parson, *Metall. Mater. Trans. A*, 2019, vol. 50A, pp. 5324–35.
33. H.-K. Park, H.-G. Kang, C.-S. Park, M.-Y. Huh, and N.-M. Hwang, *Metall. Mater. Trans. A*, 2012, vol. 43A, pp. 5218–23.
34. J. Chang, K. Takata, K. Ichitani, and E. Taleff, *Metall. Mater. Trans. A*, 2010, vol. 41A, pp. 1942–1953.
35. F. Bachmann, R. Hielscher, and H. Schaeben, *Solid State Phenom.*, 2010, vol. 160, pp. 63–68.
36. N. Bozzolo, S. Jacomet, and R. Logé, *Mater. Charact.*, 2012, vol. 70, pp. 28–32.
37. C. Kerisit, R. Logé, S. Jacomet, V. Llorca, and N. Bozzolo, *J. Microsc.*, 2013, vol. 250, pp. 189–99.
38. A. Seret, C. Moussa, M. Bernacki, J. Signorelli, and N. Bozzolo, *J. Appl. Crystallogr.*, 2019, vol. 52, pp. 548–63.
39. A. Nicolaÿ, J. Franchet, J. Cormier, H. Mansour, M. De Graef, A. Seret, and N. Bozzolo, *J. Microsc.*, 2019, vol. 73, pp. 135–47.
40. O. Engler and E. Brünger, *Matériaux & Techniques*, 2002, vol. 90, pp. 71–78.
41. P. Konijnenberg, S. Zaefferer, and D. Raabe, *Acta Mater.*, 2015, vol. 99, pp. 402–14.
42. A. Nicolaÿ, G. Fiorucci, J. Franchet, J. Cormier, and N. Bozzolo, *Acta Mater.*, 2019, vol. 174, pp. 406–17.
43. A. Ridha and W. Hutchinson, *Acta Metall.*, 1982, vol. 30, pp. 1929–39.
44. O. Daaland and E. Nes, *Acta Mater.*, 1996, vol. 44, pp. 1389–11.
45. H. Vatne, R. Shahani, and E. Nes, *Acta Mater.*, 1995, vol. 44, pp. 4447–62.
46. I. Samajdar and R. Doherty, *Acta Mater.*, 1998, vol. 46, pp. 3145–58.
47. M. Alvi, S. Cheong, J. Suni, H. Weiland, and A. Rollett, *Acta Mater.*, 2008, vol. 56, pp. 3098–08.
48. B. Hutchinson, *Mater. Sci. Forum*, 2012, vol. 702–703, pp. 3–10.
49. B. DeCost, E. Holm, *Metall. Mater. Trans. A*, 2017, vol. 48A, pp. 2771–80.
50. E. Nes, N. Ryum, and O. Hunderi, *Acta Metall.*, 1985, vol. 33, pp. 11–22.
51. C. Sinclair, F. Robaut, L. Maniguet, J.-D. Mithieux, J.-H. Schmitt, and Y. Brechet, *Adv. Eng. Mater.*, 2003, vol. 5, pp. 570–74.
52. S. Tangen, K. Sjølstad, T. Furu, and E. Nes, *Metall. Mater. Trans. A*, 2010, vol. 41A, pp. 2970–83.
53. N. Bozzolo, G. Sawina, F. Gerspach, K. Sztwiertnia, A. Rollett, and F. Wagner, *Mater. Sci. Forum*, 2007, vol. 558–559, pp. 863–68.
54. S. Wright, *Mater. Sci. Technol.*, 2006, vol. 22, pp. 1287–97.
55. N. Bozzolo, N. Dewobroto, T. Grosdidier, and F. Wagner, *Mater. Sci. Eng. A*, 2005, vol. 397, pp. 346–55.
56. Y. Zhang, A Godfrey, Q Liu, W Liu, and D Juul Jensen, *Acta Mater.*, 2009, vol. 57, pp. 2631–39.
57. C.-S. Park, H.-K. Park, H.-S. Shim, T.-W. Na, C.-H. Han, and N.-M. Hwang, *Philos. Mag. Lett.*, 2015, vol. 95, pp. 220–28.
58. N. Pedrazas, T. Buchheit, E. Holm, and E. Taleff, *Mater. Sci. Eng. A*, 2014, vol. 610, pp. 76–84.
59. H. Park, D.-Y. Kim, N.-M. Hwang, Y.-C. Joo, C.-H. Han, and J.-K. Kim, *J. Appl. Phys.*, 2004, vol. 95, pp. 5515–21.
60. K.-J. Ko, J.-T. Park, J.-K. Kim, and N.-M. Hwang, *Scripta Mater.*, 2008, vol. 59, pp. 764–67.
61. J. Koo, D. Yoon, and M. Henry, *Metall. Mater. Trans. A*, 2000, vol. 31A, pp. 1489–91.
62. D. Brandon, *Acta Metall.*, 1966, vol. 14, pp. 1479–84.
63. G. Rohrer, *J. Mater. Sci.*, 2011, vol. 46, pp. 5881–95.
64. S. Van Boxel, S. Schmidt, W. Ludwig, Y. Zhang, D.J. Jensen, and W. Pantleon, *Mater. Trans.*, 2014, vol. 55, pp. 128–36.